New tests of the universality of free fall

Y. Su, B. R. Heckel, E. G. Adelberger, J. H. Gundlach, M. Harris, G. L. Smith, and H. E. Swanson
Department of Physics FM-15, University of Washington, Seattle, Washington 98195
(Received 2 March 1994)

We use a continuously rotating torsion balance to make new tests of the universality of free fall (UFF). We study differential accelerations of Be-Cu and Be-Al test-body pairs in the fields of Earth, the Sun, our Galaxy, and in the direction of the cosmic microwave dipole. We also compare the acceleration towards the Sun and our galactic center of Cu and single-crystal Si in an Al shell (this pair of bodies approximates the elemental compositions of Earth's core and the Moon or Earth's crust, respectively). In terms of the classic UFF parameter η, our Earth-source results are $\eta(\mathrm{Be,Cu}) = (-1.9 \pm 2.5) \times 10^{-12}$ and $\eta(\mathrm{Be,Al}) = (-0.2 \pm 2.8) \times 10^{-12}$ where all errors are 1σ. Thus our limit on UFF violation for Be and a composite Al/Cu body is $\eta = (-1.1 \pm 1.9) \times 10^{-12}$. Our solar-source results are $\Delta a(\mathrm{Be,Cu}) = (-3.0 \pm 3.6) \times 10^{-12}$ cm/s^2, $\Delta a(\mathrm{Be,Al}) = (+2.4 \pm 5.8) \times 10^{-12}$ cm/s^2, and $\Delta a(\mathrm{Si/Al,Cu}) = (+3.0 \pm 4.0) \times 10^{-12}$ cm/s^2. This latter result, when added to the lunar laser-ranging result that senses both composition-dependent forces and gravitational binding-energy anomalies, yields a nearly model-independent test of the UFF for gravitational binding energy at the 1% level. A fivefold tighter limit follows if composition-dependent interactions are restricted to vector forces. Our galactic-source results test the UFF for ordinary matter attracted toward dark matter, yielding $\eta^{\mathrm{DM}}(\mathrm{Be,Cu}) = (-1.3 \pm 0.9) \times 10^{-3}$, $\eta^{\mathrm{DM}}(\mathrm{Be,Al}) = (+1.8 \pm 1.4) \times 10^{-3}$ and $\eta^{\mathrm{DM}}(\mathrm{Si/Al,Cu}) = (+0.7 \pm 1.0) \times 10^{-3}$. This provides laboratory confirmation of the usual assumption that gravity is the dominant long-range interaction between dark and luminous matter. We also test Weber's claim that solar neutrinos scatter coherently from single crystals with cross sections $\sim 10^{23}$ times larger than the generally accepted value and rule out the existence of such cross sections.

PACS number(s): 04.80.−y, 14.80.−j, 95.35.+d

I. INTRODUCTION

The universality of free fall (UFF) asserts that a point test body, shielded from all known interactions except gravity, has an acceleration that depends only on its location. The UFF is closely related to the gravitational equivalence principle, which requires an exact equality between gravitational mass m_g and inertial mass m_i and therefore the universality of gravitational acceleration. Experimental tests of the UFF have two aspects–they can be viewed as tests of the equivalence principle or as probes for new interactions that violate the UFF.

The classic modern tests [1,2] of the UFF placed upper limits on the parameter

$$\eta(A,B) = \frac{\Delta a}{a_g} = 2\frac{(m_g/m_i)_A - (m_g/m_i)_B}{(m_g/m_i)_A + (m_g/m_i)_B} \qquad (1)$$

by using torsion balances to measure the differential accelerations, $\Delta a = a_A - a_B$, of laboratory test bodies A and B toward the Sun. There were strong experimental reasons for using the *Sun* rather than *Earth* as the attracting body, even though the UFF-violating signal for a given η is about 3 times weaker in experiments where the Sun is the attracting body [3]. The disadvantage of the weaker solar signal is outweighed by the systematic advantages of the solar source. The great distance to the Sun effectively eliminates problems from gravity gradients and magnetism, and the Sun's motion modulates the signal from a laboratory-fixed apparatus, avoiding the rotation of a delicate instrument required in torsion-balance experiments that use Earth as the attracting body.

However, one pays a price for these experimental advantages: A UFF-violating interaction with a range significantly less than 1.5×10^{11} m would be essentially undetectable in solar experiments. We expect a UFF-violating interaction to arise from the exchange of scalar or vector bosons of mass m_b, leading to a potential energy between two point objects of the form

$$V_{AB}(r) = \mp\frac{g^2}{4\pi}(q_5)_A(q_5)_B\frac{e^{-r/\lambda}}{r}\ , \qquad (2)$$

where g is a coupling constant, q_5 denotes the "charge" of the body, $\lambda = \hbar/m_b c$ is the interaction range which could, in principle, have any value ranging from the Planck length to infinity, and the minus and plus signs refer to interactions mediated by scalar or vector bosons, respectively.

The interaction specified in Eq. (2) would produce a differential acceleration of closely spaced point test bodies A and B toward a point source S which may be written as

$$\frac{\Delta\vec{a}}{a_g} = -\alpha_5\,\Delta\left(\frac{q_5}{\mu}\right)\left(\frac{q_5}{\mu}\right)_S\left(1+\frac{r}{\lambda}\right)e^{-r/\lambda}\,\hat{r}\ , \qquad (3)$$

where $\Delta\vec{a} = \vec{a}_A - \vec{a}_B$, $\alpha_5 = \mp g^2/(4\pi u^2 G)$, u denotes the atomic mass unit, μ represents mass in amu, and a_g is the gravitational acceleration toward the source. As expected the differential acceleration is proportional to the difference in "charge"-to-mass ratios of the test bod-

ies, $\Delta(q_5/\mu) = (q_5/\mu)_A - (q_5/\mu)_B$, times the "charge"-to-mass ratio of the source, $(q_5/\mu)_S$. For an extended source, the differential acceleration becomes

$$\Delta\vec{a} = \alpha_5 \Delta\left(\frac{q_5}{\mu}\right)\left\langle\frac{q_5}{\mu}\right\rangle_S \vec{J}(\lambda) , \quad (4)$$

where the term in the anglular brackets is the average "charge"-to-mass ratio of the source, and the source strength

$$\vec{J}(\lambda) = G\,\vec{\nabla}_r \int \rho(\vec{r}\,')\frac{e^{-|\vec{r}-\vec{r}\,'|/\lambda}}{|\vec{r}-\vec{r}\,'|}d^3r' \quad (5)$$

is integrated over the density ρ of the source.

We have no bias as to what might constitute the "charge" of a UFF-violating interaction and designed our experiment accordingly. However, vector interactions coupled to charges of $q_5 = B$, $q_5 = L$, $q_5 = B - L$, and $q_5 = 3B + L$, where B and L are the baryon and lepton numbers, respectively, may have some special interest because B and L are conserved within the accuracy of existing experiments, $B - L$ is conserved in grand unified theories that do not conserve B and L individually, and $3B+L$ simply counts the number of elementary fermions. As a result we typically discuss our results in terms of the most general vector charge of electrically neutral, stable matter

$$q_5 = B\cos\theta_5 + L\sin\theta_5 , \quad (6)$$

where θ_5 is a parameter that may have any value from $-\pi/2$ to $\pi/2$.

Theories containing scalar interactions are probably the most natural extensions of general relativity, the "standard model" of gravitation. For example, all string theories predict a scalar partner of the tensor graviton (the dilaton), both of which arise as products of left-moving and right-moving excitations of the string. A massless dilaton is usually rejected because it would produce large violations of the UFF. However, Damour and Polyakov [4] discuss a string theory scenario containing a massless dilaton that nevertheless generates a very small violation of the UFF. They argue that string-loop modifications of the dilaton-matter couplings may provide a mechanism whereby cosmological evolution drives the dilaton to couple to matter so weakly that it could not have been detected in existing UFF experiments. From our standpoint of interpreting experimental constraints, scalar interactions couple to charges that cannot be specified as simply as is possible for vector interactions, but a tree-level approximation for the scalar charge leads to an expression for q_5 that is similar to Eq. (6). We emphasize that scalar "charges" (three-space integrals over the Lorentz scalar charge density), unlike vector charges, are neither conserved nor Lorentz invariants; it is only at the tree level that the scalar charge of a complex body is the sum of the scalar charges of its constituents.

In this paper, we present new results that complement in several ways the classic work of Refs. [1] and [2]. First, we studied differential accelerations in the field of Earth so that we could probe UFF-violating interactions with λ's ranging from 1 m to infinity. Second, the elemental compositions of our test-body pairs (Be-Al, Be-Cu) were quite different from those used previously, Al-Au [1] and Al-Pt [2], to preclude the possibility that a UFF-violating interaction was not detected because $\Delta(q_5/\mu)$ happened to be very small for the similar test body pairs used in the two solar experiments. Third, we analyzed our data to extract limits on differential acceleration toward the center of our Galaxy as well as in the frame in which the cosmic microwave background is isotropic. These latter two measurements were undertaken to test the UFF for ordinary matter falling toward dark matter that is believed to account for most of the observed large-scale astronomical accelerations [5,6].

In addition we compared the accelerations toward the sun of Cu and composite Si/Al test bodies. We were motivated by Nordtvedt's observation [7] that the highly precise lunar laser-ranging test of the UFF for Earth and the Moon falling toward the Sun [8] is actually two tests in one: a test of the UFF for gravitational binding energy (gravitational binding energy reduces Earth's mass by about 5 parts in 10^{10} but is much less important in the Moon) and a probe for composition-dependent nongravitational interactions (Earth has a sizable Fe/Ni core while the Moon does not). One can separate these two tests, and eliminate the possibility that a composition-dependent interaction masks a gravitational binding energy anomaly, by comparing the accelerations toward the Sun of "scale-models" of Earth and the Moon that have the same or similar compositions as the real Earth and Moon but negligible gravitational self-energies. We approximated this test: Our Si/Al bodies simulated the elemental compositions of Earth's crust and the Moon, while Earth's core was simulated by the Cu bodies.

Finally, because our composite Si/Al bodies contained dynamically perfect single crystals of Si, it was possible, as a by-product of our work, to test Weber's claim [9] that solar neutrinos scatter coherently from a single crystal with cross sections over $\sim 10^{23}$ times larger than the generally accepted value [10]. No evidence for such enhanced cross sections was observed.

The basic principles and many aspects of our instrument and analysis methods have already been presented in some detail [11]. In this paper we concentrate on those features of our instrument and analysis methods that have been upgraded since the publication of Ref. [11].

II. THE EÖT-WASH ROTATING TORSION BALANCE

A. General description

The Eöt-Wash continuously rotating torsion balance operates in a laboratory excavated from a hillside on the University of Washington campus with the balance ≈ 1.7 m from an exterior wall facing the hill. This site provides a reasonably strong source for Yukawa interactions with ranges down to about 1 m. Figure 1 shows a side view of the instrument. A highly symmetric torsion pendulum is freely suspended in vacuum from a 20 μm

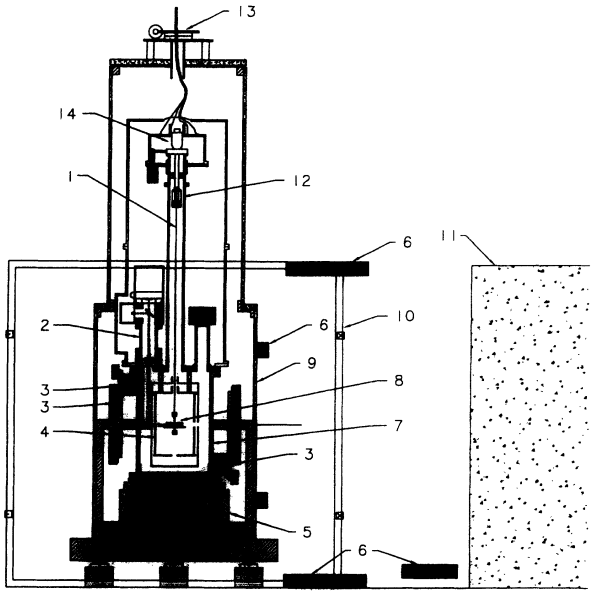

FIG. 1. Cross section of Eöt-Wash apparatus. 1, torsion fiber; 2, autocollimator; 3, rotateable gravity-gradient compensators; 4, magnetic shields; 5, turntable; 6, stationary gravity-gradient compensators; 7, vacuum vessel; 8, pendulum; 9, outer heat shield; 10, Helmholtz coils; 11, concrete block; 12, damper; 13, corotating cable clamp; 14, upper fiber attachment mechanism. The concrete block abuts the hillside wall of the laboratory and is 1.23 m high.

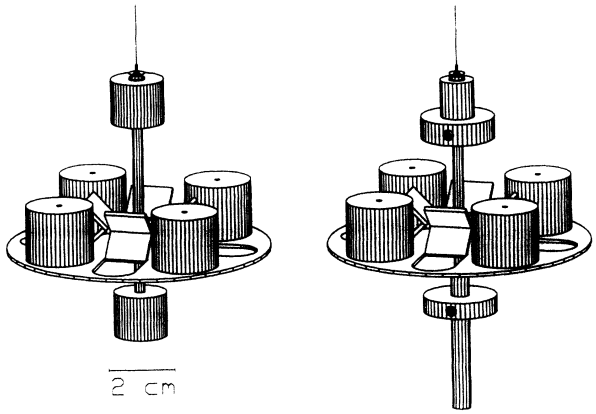

FIG. 2. Details of the two torsion pendulums used in this work. The pendulums have extensive symmetry to minimize spurious effects, and the test bodies themselves can be interchanged on the pendulum tray to further discriminate against false effects. Left: the pendulum (described in Ref. [11]) used in the Al-Be experiment and part of the Cu-Be experiment. Right: the pendulum used for part of the Cu-Be experiment and the Si/Al-Cu experiment. The masses on the upper and lower ends of the central axle minimize the pendulum's $\bar{q}_{20}$ and $\bar{q}_{30}$ moments. These two masses contain trim screws that are used to null the $\bar{q}_{21}$ moment arising from small machining imperfections.

diameter 0.8 m long Au-coated W fiber. Torques on the pendulum are monitored by an optical autocollimator system with high sensitivity to torsional excursions, but essentially no sensitivity to the "swing" and "wobble" modes of the pendulum. The pendulum and its associated apparatus are mounted on a turntable that rotates continuously around a vertical axis with a period $\tau_{\rm can}$, long compared to the free torsional oscillation period of the pendulum, $\tau_0 \approx 695$ s. The rotating pendulum is located at the center of a set of stationary masses that "flatten" the local gravitational field and a set of three-axis Helmholtz coils that cancel the ambient magnetic field. In addition the pendulum is surrounded by three nested corotating magnetic shields that attenuate the residual laboratory-fixed magnetic field by a large factor. The rotating apparatus is enclosed in a hermetic thermal shield that is maintained at a constant temperature and the entire apparatus is contained in a small, heavily insulated room that is itself kept at a constant temperature by a separate controller system.

Figure 2 shows the pendulum in more detail. The pendulum employs symmetry to make it as difficult as possible for spurious effects to favor one test body over another. The pendulum contains four cylindrical test bodies, two each of two different materials. The test bodies are normally configured as a composition dipole, but can be arranged as a quadrupole to test for systematic errors. All test bodies have the same outside dimensions, identical masses, and vanishing mass quadrupole moments. The test bodies are precisely positioned in a "tray" that also contains two passive masses (discussed below) and four mirrors, any one of which can be used by the autocollimator. Thus the tray and fiber suspension system may have any of four equally spaced angles with respect to the rest of the rotating apparatus, and the composition dipole itself can have any of four configurations on the tray. This freedom to break any correlation between the orientation of the composition dipole and the angle of the turntable, or of the tray and suspension fiber, has proven to be very useful in suppressing systematic errors. The entire pendulum, including the mirrors, test bodies, and suspension fiber, is coated with Au as is the innermost magnetic shield that surrounds the pendulum.

B. Test bodies

Our test bodies are shown in cross section in Fig. 3 and their properties are listed in Table I. The Be, Al,

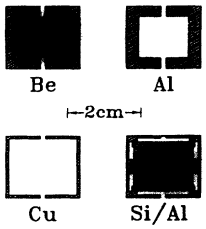

FIG. 3. Cross-sectional views of the test bodies. The symmetry axes of the cylindrical bodies lie vertically in the plane of the page.

TABLE I. Some properties of the test bodies.

Property	Be body	Al body	Cu body[a]	Cu′ body[b]	Si/Al body
Mass[c] (g)	10.0414(5)	10.0414(5)	10.0414(5)	10.0438(5)	10.0432(5)[d]
$\bar{q}_{20}$ (g cm^2)	-1.6×10^{-4}	-1.1×10^{-3}	1.4×10^{-2}	1.4×10^{-2}	1.6×10^{-2}
$\bar{q}_{40}$ (g cm^4)	-1.2	-1.6	-2.4	-2.4	-1.2
B/μ	0.998648	1.000684	1.001117	1.001117	1.000772
L/μ	0.443844	0.481811	0.456365	0.456365	0.492162

[a]Used with the Be body.
[b]Used with the Si/Al body.
[c]Buoyancy corrected.
[d]Consists of 6.2967 g of Si and 3.7465 g of Al.

and Cu bodies were those used in Ref. [11]. Before beginning the Si/Al-Cu measurements the Cu bodies were given new Au coatings so that their weights more closely matched those of the Si/Al bodies; these recoated bodies are called Cu′. The Si/Al test bodies consisted of dynamically perfect single-crystal Si cylinders contained inside Au-coated Al shells whose outside dimensions were the same as those of our other test bodies. The 111 axes of the Si crystals were parallel to the symmetry axes of the cylinders.

C. UFF-violating signal

As the turntable rotates, a laboratory-fixed differential acceleration $\Delta\vec{a}$ of the test bodies will produce a small angular deflection of the pendulum, θ, that varies harmonically as a function of turntable angle ϕ:

$$\theta(\phi) = \Delta a_\perp \frac{ms}{\kappa}\sin(\phi_0-\phi-\delta) \tag{7}$$

$$= c_1^{\sin}(\delta)\sin\phi + c_1^{\cos}(\delta)\cos\phi\ , \tag{8}$$

where $\Delta a_\perp$ is the horizontal component of the differential acceleration vector, m is the mass of an individual test body, s is the separation of two adjacent test bodies, δ the laboratory angle of the composition dipole when $\phi=0$, κ is the torsional spring constant of the fiber, and ϕ_0 denotes the laboratory azimuthal angle of $\Delta\vec{a}$ when $\delta=0$. [In Eq. (7) we have, for simplicity, neglected the attenuation and phase shift arising from the inertia of the pendulum. Our results given below are always corrected for this effect.] Because essentially all of our systematic effects depend on either the angle of the *turntable* or the orientation of the pendulum *tray* rather than on the direction of the test-body *composition dipole*, we formed our UFF-violating signal by taking equal amounts of data with various values of δ and combining the resulting $c_1^{\sin}$ and $c_1^{\cos}$ coefficients in such a way that systematic effects not explicitly associated with the test bodies themselves (such as irregularities in the turntable drive, gravity-gradient torques arising from small distortions of the pendulum tray, etc.) tended to cancel, while a true UFF-violating signal would add coherently.

In Secs. II D–II F below we discuss the major improvements made to our instrument since the publication of Ref. [11].

D. Control of the rotation rate

It was essential that the turntable rotation rate be as constant as possible because variations in this rate would twist the suspension fiber and produce an autocollimator signal. Prior to taking the new data reported in this paper, we installed an improved rotation-rate controller. This system compared the pulse train from a computer-controlled crystal oscillator to the pulse stream from a 900 000 pulse/revolution optical shaft encoder mounted on the turntable, and drove the turntable motor in such a way as to phase lock the two pulse trains. The effectiveness of this device is shown in Fig. 4. After the rate controller was installed our torsional noise dropped close to the thermal limit (see Fig. 5): The mean torsional amplitude of the rotating pendulum is now about 1.6 μrad, only 50% larger than the thermal value of 1.1 μrad. As shown in Fig. 5, the torsional amplitude when the turntable is rotating is very close to that observed when the apparatus is stationary.

E. Gravity gradient measurement and compensation

Gravitational gradients coupled to pendulum imperfections are one of the dominant systematic effects in our instrument, and so we discuss these in some detail.

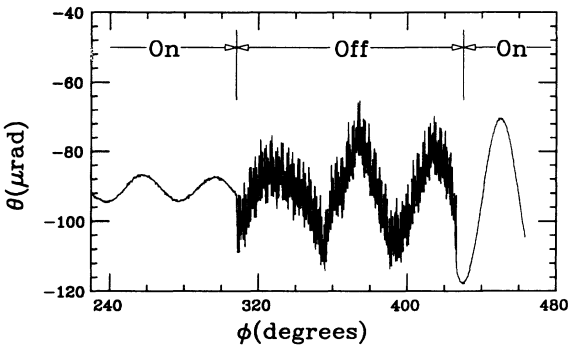

FIG. 4. Effectiveness of the turntable rotation rate controller. The feedback was switched off and then on again, to demonstrate the effect of phase locking the shaft-encoder output to a crystal oscillator. Each high-frequency oscillation is due to one rotation of the worm gear in the turntable drive. Note that the torsional oscillation was "pumped up" during the time when the feedback was off.

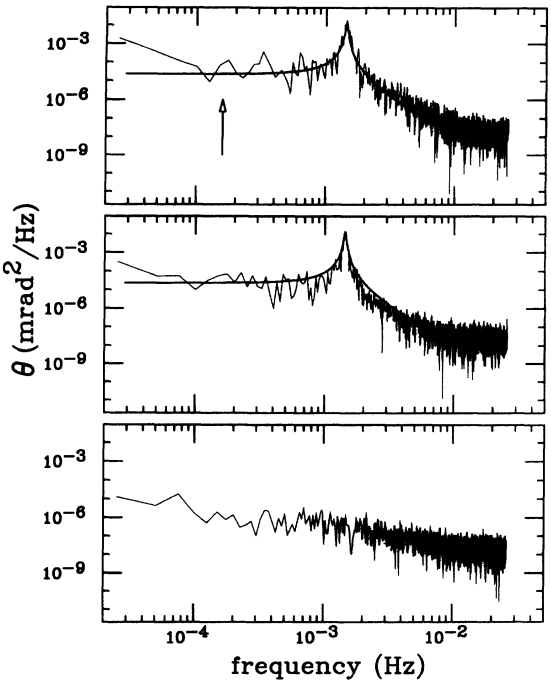

FIG. 5. Spectral power densities of the angular deflection signal. Top panel: turntable rotating; the arrow shows the frequency of our signal. Center panel: turntable stationary. Bottom panel: electronic noise observed when the autocollimator viewed a corner reflector instead of the pendulum. Note that the noise while rotating is very close to the noise when the turntable is stationary. The smooth curves in the upper two plots show the predicted thermal noise levels plus the noise "floor" from the electronics.

1. *Formalism*

The gravitational potential energy of our pendulum can be written as

$$W = -4\pi G \sum_{l=0}^{\infty} \frac{1}{2l+1} \sum_{m=-l}^{+l} q_{lm} Q_{lm} \ , \tag{9}$$

where the multipole moments

$$q_{lm} = \int \rho_p(\vec{r}) r^l Y^*_{lm}(\hat{r}) d^3r \tag{10}$$

and the multipole fields

$$Q_{lm} = \int \rho_s(\vec{r}') r'^{-(l+1)} Y_{lm}(\hat{r}') d^3r' \tag{11}$$

are integrated over the source and the pendulum, respectively. We assume that the $\hat{z}$ axis of our coordinate system coincides with the turntable rotation axis. If the pendulum is rotated about $\hat{z}$ at a frequency ω so that $\phi = \omega t$, then

$$q_{lm} = q_{lm}(t) = \bar{q}_{lm} e^{-im\omega t} \ , \tag{12}$$

where $\bar{q}_{lm}$ is calculated in a body-fixed frame [for the moment we assume the pendulum center of mass (c.m.) lies on the $\hat{z}$ axis so that $\bar{q}_{lm}$ is computed about the pendulum c.m.].

The gravitational torque on the pendulum is then

$$T_g = -\frac{\partial W}{\partial \phi} = -4\pi i G \sum_{l=0}^{\infty} \frac{1}{2l+1} \sum_{m=-l}^{+l} m \bar{q}_{lm} Q_{lm} \times e^{-im\omega t} \ , \tag{13}$$

so that gravity will produce an $m\omega$ signal if $\bar{q}_{lm} Q_{lm} \neq 0$. In particular, if the $\bar{q}_{l1} Q_{l1}$ product does not vanish, gravity will produce a spurious 1ω signal that could mimic a UFF violation.

Equation (13) converges as $(r/R)^l$ where r is a typical dimension of the pendulum and R is a characteristic distance from the pendulum to the closest source. Because $r/R \leq 1/10$, gravitational torques arise predominantly from low l terms. However, the $\bar{q}_{11}$ moment vanishes for a pendulum suspended from a perfectly flexible fiber, and so the most troublesome effects come from the $m = 1$ terms with $l \geq 2$. Although our pendulum was designed so that the first $m = 1$ moment nominally occurred in $l = 5$ order (because the q_{40} moments of the individual test bodies were not identical), small imperfections generated lower-order moments that caused the dominant systematic errors.

We must also allow for misalignments of the torsion pendulum and consider two such misalignments: an off-center attachment of the torsion fiber to the pendulum and a displacement between the fiber and the rotation axis of the turntable. If the fiber is not attached exactly on the pendulum symmetry axis, the pendulum will hang "tipped" and acquire effective moments

$$\tilde{q}_{lm} = \sum_{m'=-l}^{l} \bar{q}_{lm'} \mathcal{D}^l_{m',m}(\alpha, \beta, \gamma) \ , \tag{14}$$

where $\mathcal{D}$ is a rotation function [12] and α, β, and γ are Euler angles that describe the "tip" of the pendulum. The leading order effect of pendulum tip is to generate a $\tilde{q}_{l1}$ moment from $\bar{q}_{l0}$ and $\bar{q}_{l2}$ moments. For this reason, the pendulum was designed to have very small $\bar{q}_{20}$, $\bar{q}_{22}$, $\bar{q}_{30}$, and $\bar{q}_{32}$ moments.

If the turntable axis $\hat{z}$ does not pass through the pendulum c.m., additional torques arise because, as the turntable rotates, the pendulum travels in a small circle in the laboratory frame (the frame in which the Q_{lm} are computed). This leads to an effective moment

$$\tilde{q}_{LM} = \sum_{l,m,l',m'} \sqrt{\frac{4\pi(2L+1)!}{(2l'+1)!(2l+1)!}} (r')^{l'} Y^*_{l'm'}(\hat{r'}) \ \bar{q}_{lm} e^{-im\phi} C(l', m', l, m, L, M) \delta_{l+l',L} \ , \tag{15}$$

where $\vec{r}'$ is the vector from the pendulum c.m. to the origin of the coordinate system and C is a Clebsch-Gordan coefficient. In this case the gravitational potential energy is

$$W = -4\pi G \sum_{L,M} \frac{Q_{LM}}{2L+1} \sum_{l,m,l',m'} \sqrt{\frac{4\pi(2L+1)!}{(2l'+1)!(2l+1)!}} (r')^{l'} Y^*_{l'm'}(\hat{r}') \, \bar{q}_{lm} e^{-im\phi} C(l',m',l,m,L,M) \delta_{l+l',L} \,. \tag{16}$$

The torque on the pendulum is found by differentiating W with respect to the pendulum angle ϕ, keeping $\vec{r}'$ fixed. (Although $\vec{r}'$, the coordinate of the pendulum c.m., varies as the turntable rotates, variations of W due to changes in $\vec{r}'$ do not produce any torque about the fiber.) Then we allow $\vec{r}'$ to vary as

$$Y^*_{l'm'}(\hat{r}')(r')^{l'} = \bar{\epsilon}_{l'm'} e^{-im'\phi} \,, \tag{17}$$

where $\bar{\epsilon}_{l'm'}$ is the displacement term when $\phi = 0$. Therefore

$$T_g = -4\pi i G \sum_{L,M} \frac{Q_{LM}}{2L+1} \sum_{l,m,l',m'} m \sqrt{\frac{4\pi(2L+1)!}{(2l'+1)!(2l+1)!}} C(l',m',l,m,L,M) \bar{\epsilon}_{l'm'} \bar{q}_{lm} e^{-i(m+m')\omega t} \delta_{l+l',L} \,. \tag{18}$$

For an ideal but off-centered pendulum, whose lowest $m \neq 0$ moment is nominally $\bar{q}_{44}$, the leading order effect couples to Q_{53} and Q_{55} fields producing 3ω and 5ω signals, but without affecting the 1ω signal that is our UFF-violating signature. Because the actual pendulum has a stray $\bar{q}_{22}$ moment which can couple to a Q_{31} field and produce a 1ω signal, it is important to center the pendulum with reasonable accuracy. We centered the fiber to within 0.13 mm of the turntable rotation axis.

A program MULTI was developed to assist us in designing the pendulums and gravity-gradient compensators. MULTI computes the gravitational and Yukawa multipole moments and fields (the Yukawa moments and fields are defined in Ref. [11]) of mass distributions assembled from a menu of basic shapes such as cylinders, cones, and plates of various shapes. A second program MOVE then was used to translate and rotate the multipole moments calculated by MULTI.

2. *Measuring the gravity gradients*

We reduced gravitational systematic errors by measuring and then minimizing both the stray $\bar{q}_{l1}$ moments of the pendulum and the Q_{l1} field gradients. The Q_{lm} fields were measured by replacing the normal test bodies with special gradiometer test bodies that gave the pendulum large, known $\bar{q}_{lm}$ moments, and observing the resulting $m\omega$ signals. An ideal gradiometer pendulum has a large $\bar{q}_{lm}$ moment, negligible values for all other moments, and a vanishing composition dipole moment. Figure 6 shows gradiometers that were used to measure the Q_{21}, Q_{31}, and Q_{41} fields. The Q_{22} field was measured simply by removing two diagonally opposite test bodies from the normal pendulum. The gravitational properties of our gradiometers are listed in Table II and the measured laboratory gradients are shown in Table III .

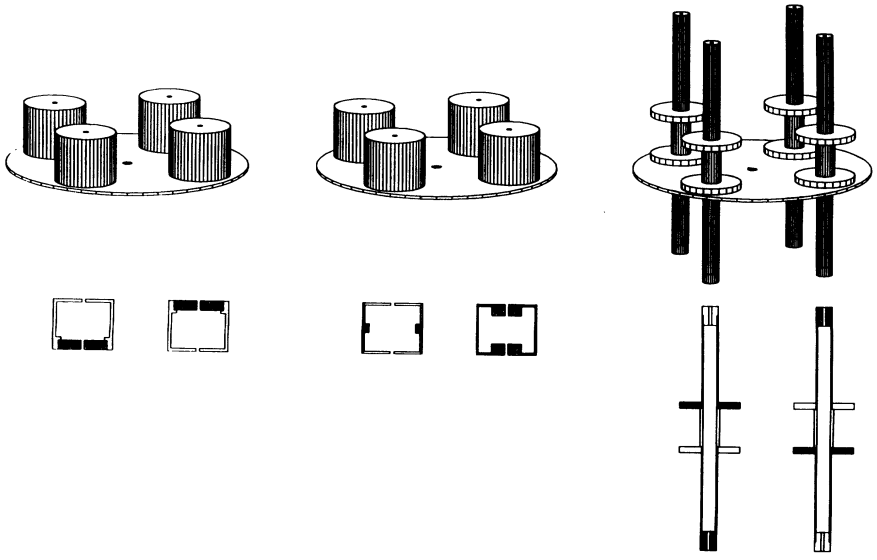

FIG. 6. Gravity gradiometers used in this work. Left: gradiometer with a large, calculable $\bar{q}_{21}$ moment that measures the laboratory Q_{21} gradient. Center: gradiometer with a large, calculable $\bar{q}_{31}$ moment that measures the laboratory Q_{31} gradient. Right: gradiometer with a large, calculable $\bar{q}_{41}$ moment that measures the laboratory Q_{41} gradient. The shaded areas in the cross-sectional views are Cu; the unshaded areas are Al.

TABLE II. Calculated gravity moments of the gradiometers.

Moment	$\bar{q}_{21}$ gradiometer	$\bar{q}_{31}$ gradiometer	$\bar{q}_{41}$ gradiometer
$\lvert\bar{q}_{21}\rvert$(g cm^2)	24.0	0	0
$\lvert\bar{q}_{31}\rvert$(g cm^3)	0	22.9	0
$\lvert\bar{q}_{41}\rvert$(g cm^4)	338	0	646
$\lvert\bar{q}_{51}\rvert$(g cm^5)	0	519	0

3. *Compensating the gravity gradients*

The gravitational field at the pendulum c.m. was "flattened" using a systematic approach based on the multipole formalism given above. The leading order gradient was found to be $Q_{21} = (-0.046 + 1.151i)$ g/cm^3 (see Fig. 7 and Table III) with uncertainties at the ± 0.002 g/cm^3 level. This agreed reasonably with calcuations based on the local mass distribution that predicted $Q_{21} = (-0.10 + 1.17i)$ g/cm^3 . We compensated this gradient by installing the Q_{21} compensators as shown in Fig. 8; these reduced the Q_{21} gradient (just after compensation) to less than 0.004 g/cm^3. Next the Q_{22} gradient, which also has a strong contribution from the hillside, was compensated using the mass distribution also shown in Fig. 8. Then the Q_{31} and finally the Q_{41} gradients were compensated in similar ways. The results of this procedure are summarized in Table III.

4. *Measuring the $\bar{q}_{lm}$ moments of the pendulum*

The $\bar{q}_{l1}$ moments of our pendulums were determined by introducing machined masses to produce large, known Q_{l1} fields and observing the change in the 1ω signal as the applied Q_{l1} field was reversed in the laboratory (see below). The calculated and measured gravitational moments of our pendulums are listed in Table IV.

5. *Zeroing the q_{21} moment of the pendulum*

Recently, we discovered that the Q_{21} gradient has seasonal variations. Figure 9 shows the Q_{21} gradient measured during a week when the annual rainy season began after a long dry spell. We found that the Q_{21} field increased with time as the rain soaked into the ground, and that the size of the effect was consistent with the measured depth of the rain-soaked layer of soil. Because it was not practical to monitor continuously the Q_{21} field, it could not be compensated to an accuracy better than

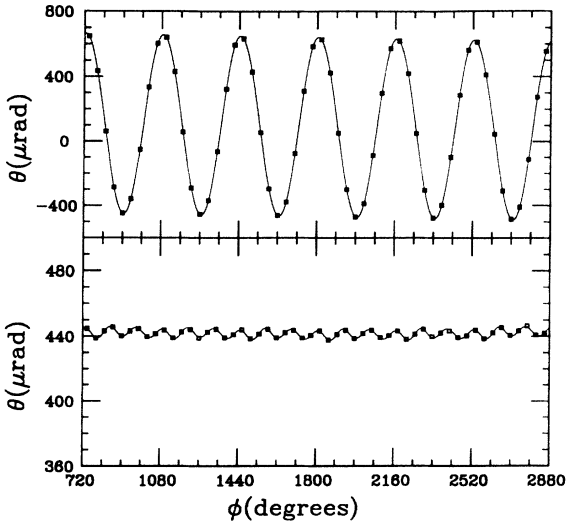

FIG. 7. Cancellation of the Q_{21} gradient. Top: the Q_{21} compensator was inverted so that it doubled the ambient gradient. The $\bar{q}_{21}$ gradiometer saw a large 1ω signal because gravity pointed in different directions at two points 8 mm apart. Bottom: the $\bar{q}_{21}$ gradiometer signal with the Q_{21} compensator in its normal position. The 1ω signal was reduced by a factor of $\approx$900, but a small 3ω signal was observed. This 3ω signal arose from the $\bar{q}_{43}$ moment of the gradiometer coupling to the small Q_{43} field of the compensator. The observed 3ω amplitude of 3.17 ± 0.08 μrad agrees reasonably with the 3.33 μrad value calculated from the known geometries of the gradiometer and compensator. (Linear drift has been subtracted from these data.)

the amount by which it fluctuates, about 0.02 g/cm^3. To limit the systematic error from $\bar{q}_{21}Q_{21}$ coupling, we had to reduce the stray $\bar{q}_{21}$ moment of the pendulum. This was done by installing two orthogonal pairs of 0.041 g Al set screws in both the top and bottom counterweights of the pendulum (see Fig. 2) and adjusting these screws to tune out the $\bar{q}_{21}$ moment of the pendulum. One turn of one pair of screws changed $\bar{q}_{21}$ by about 0.0115 g cm^2. These screws were adjusted until the 1ω signal from the tuned pendulum was below 200 nrad in the large (about 200 times normal) gradient produced by inverting the Q_{21} compensator. Therefore, in normal runs, the 1ω signal from $\bar{q}_{21}Q_{21}$ coupling is less than 1 nrad. Furthermore, most of this 1 nrad signal was independent of the direction of the composition dipole on the pendulum tray and thus further canceled in our UFF-violating signature.

TABLE III. Measured values of the gravity gradients.

Gradient	Uncompensated value	Compensated value
Q_{21} (g cm^{-3})	$(-0.046 + 1.151i)(\pm 0.002)$	$(-0.22 + 1.53i) \times 10^{-3}(\pm 0.2 \times 10^{-3})$[a]
Q_{22} (g cm^{-3})	$(0.94 - 0.22i)(\pm 0.01)$	< 0.01
Q_{31} (g cm^{-4})	$(0.14 - 1.72i) \times 10^{-3}(\pm 0.16 \times 10^{-3})$	$(0.15 - 0.11i) \times 10^{-3}(\pm 0.12 \times 10^{-3})$
Q_{41} (g cm^{-5})	$(0.8 + 7.5i) \times 10^{-5}(\pm 1.5 \times 10^{-5})$	$(2.0 + 0.8i) \times 10^{-5}(\pm 1.6 \times 10^{-5})$

[a]Varies by ± 0.02 g cm^{-3} according to the water content of the soil.

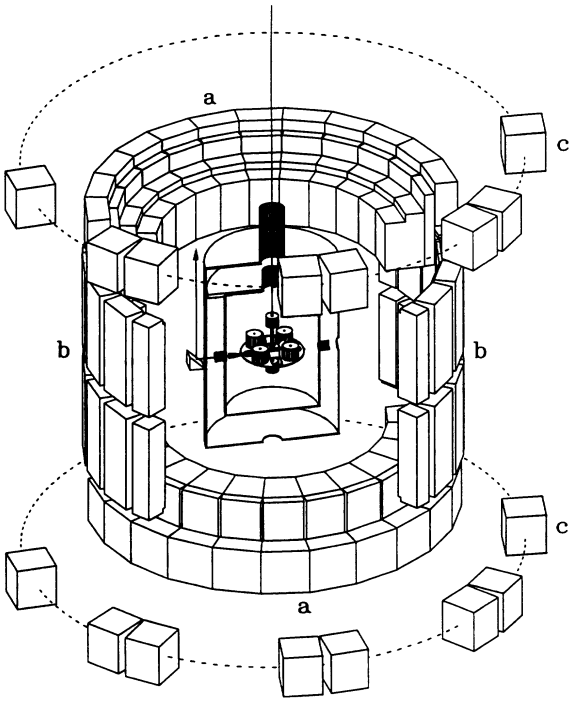

FIG. 8. Gravity-gradient compensators used to "flatten" the local gravitational field: *a*: Q_{21} compensator, *b*: Q_{22} compensator, *c*: Q_{31} compensator.

F. Additional improvements

Even though the torsional frequency of our pendulum is at least 300 times lower than the frequencies of the "swing" (0.5 Hz), "wobble" (2 Hz), "bounce" (7 Hz), and "guitar string" (~200 Hz) modes, it is desirable to damp these modes in a time short compared to a torsional period so that nonlinear effects do not transfer energy from these modes into the torsional oscillation. This was done by mounting a passive eddy-current damper on the piece joining the thicker "pre-hanger" fiber (see Ref. [11]) to the main fiber. This gave a swing mode damping time of 400 but had a negligible effect on the torsional mode,

TABLE IV. Gravity moments of the Cu-Be pendulum shown in the right half of Fig. 2. Values for the pendulum with Al-Be test bodies differ slightly.

Moment	Calculated value	Measured value[a]
$\lvert\overline{q}_{20}\rvert$ (g cm^2)	−1.46	
$\lvert\overline{q}_{21}\rvert$ (g cm^2)		0.0054 ± 0.0031
$\lvert\overline{q}_{22}\rvert$ (g cm^2)		0.041 ± 0.021
$\lvert\overline{q}_{30}\rvert$ (g cm^3)	33.8	
$\lvert\overline{q}_{31}\rvert$ (g cm^3)		0.48 ± 0.29
$\lvert\overline{q}_{40}\rvert$ (g cm^4)	2837	
$\lvert\overline{q}_{41}\rvert$ (g cm^4)		7.7 ± 4.3
$\lvert\overline{q}_{44}\rvert$ (g cm^4)	−1016	

[a]The quoted uncertainty indicates the spread in values over all configurations. The errors of the individual measurements are smaller.

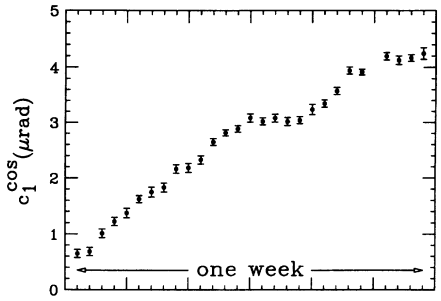

FIG. 9. Variation of the Q_{21} gradient as rain water soaked into the ground. The vertical axis shows the 1ω gradiometer signal.

whose damping time of about 5500 s (see Fig. 10) was limited by the residual gas pressure.

Thermal shielding was improved by adding an air-tight Al shell that enclosed the fiber column, upper fiber attachment, and the autocollimator; this shell reduced the 1ω variations of the internal temperature sensors by a factor of about 10. The turntable bearing used in Ref. [11] was rebuilt before taking the data reported here; this largely eliminated the 3ω variation in the orientation of the rotation axis (compare Fig. 11 to Fig. 20 of Ref. [11]). After taking the Be-Al and Be-Cu data and before starting the experiment with the Si/Al test bodies, the autocollimator was improved by replacing the light-emitting diode (LED) and/or optical-fiber source discussed in Ref. [11] with a direct diode laser.

III. SIGNAL EXTRACTION

Signals from the autocollimator, 2 orthogonal electronic tilt sensors mounted on the rotating apparatus,

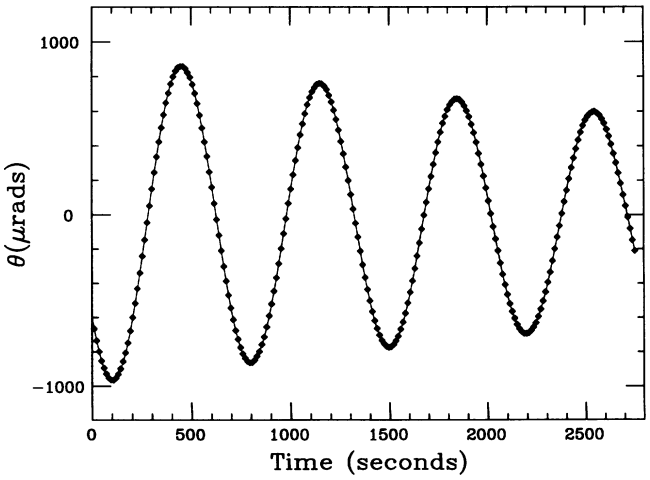

FIG. 10. Dynamic calibration based on an abrupt change of the turntable rotation rate by 8.72 μrad/s at $t = -70.5$ s. The pendulum response to this change calibrated the angle and torque scales. The data are shown as small diamonds. The curve is the best damped oscillation fit.

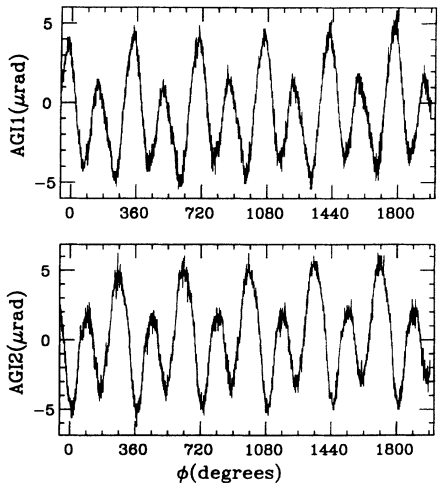

FIG. 11. Readings from two orthogonal tilt sensors mounted on the rotating instrument. Fourier analysis of these data reveal 1ω, 2ω, and 3ω signals of 2.56, 4.55, and 0.35 μrad, respectively. The results differ from those shown in Fig. 20 of Ref. [11] because the bearing was rebuilt after publication of that paper.

2 orthogonal optical sensors that monitored the position of the suspension fiber in the can frame, and 12 temperature sensors were digitized in a 16-bit analogue-to-digital converter (ADC) and recorded, together with the shaft encoder digital output, every $\approx$ 19.3 s by a small computer. The sampling time was selected so that 36 data

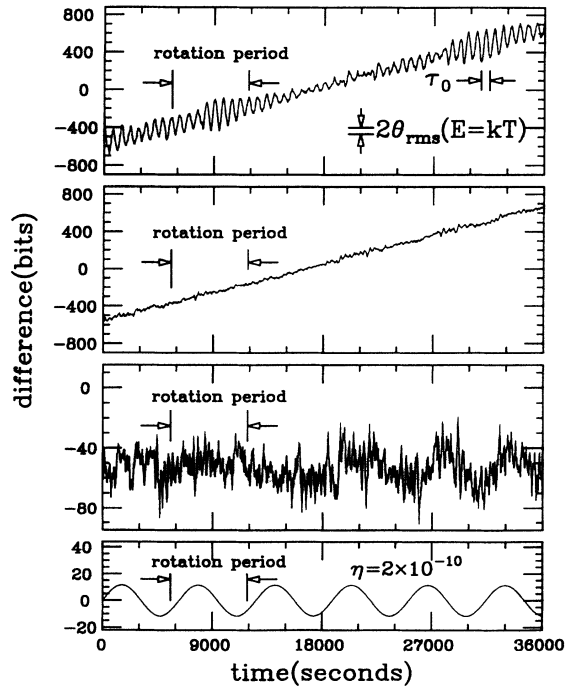

FIG. 12. Top panel: raw autocollimator readings. Upper middle panel: after applying the filter that suppressed free torsional oscillations. Lower middle panel: after applying the filter that suppresses fiber drift. Bottom panel: expected signal from a UFF-violating interaction with $\eta = 2 \times 10^{-10}$.

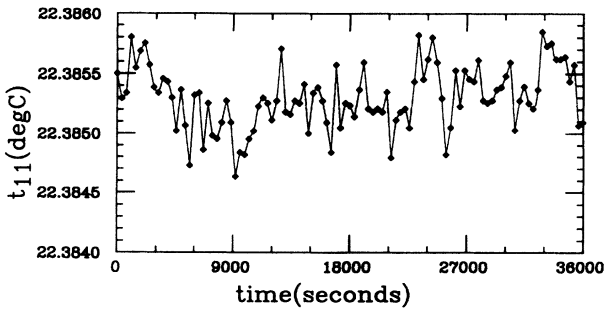

FIG. 13. Readings from a temperature sensor mounted on the autocollimator.

points were recorded for each torsional period (about 695 s). This period changed by about 0.4% when different test-body pairs (with differing moments of inertia) were installed. The turntable rotation rate was adjusted so that an integral number of torsion periods (8 or 9) occurred during one revolution of the apparatus. Typical data from the tilt sensors, autocollimator, and a temperature monitor as functions of time are shown in Figs. 11, 12, and 13, respectively.

The most prominent features of the raw autocollimator data are the steady drift in the readings (due to a slow, thermally activated drift in the fiber) and the damped torsional oscillations driven by turntable imperfections, thermal effects, and seismic disturbances. By comparing the upper panel of Fig. 12 to Fig. 7 of Ref. [11], one can see the improvement arising from the turntable rate-control feedback.

As our data analysis procedures now differ from those used in Ref. [11], we discuss our current methods in some detail.

A. Analysis of differential accelerations in Earth's field

The raw data, a sample of which is shown in the top panel of Fig. 12, consisted of series of measurements of the torsional deflection θ as a function of turntable angle ϕ. To extract the 1ω signal from $\theta(\phi)$ data, we first suppressed the torsional oscillation by averaging pairs of data points that are 180° apart in *torsional* phase. The effect of this filter is shown in the center panel of Fig. 12. Then we suppressed fiber drift and all even harmonics of the turntable rotation frequency by subtracting pairs of data points that are 180° apart in the *turntable* phase: The results of this are shown in the bottom panel of Fig. 12. These simple operations produced filtered data $\theta_f(\phi)$. The filtered data were then corrected for the instantaneous value of the tilt as measured by the two orthogonal level sensors to yield the filtered, tilt-corrected deflections:

$$\bar{\theta}(\phi) = \theta_f(\phi) - r_1 R_{\mathrm{AGI1}_f}(\phi) - r_2 R_{\mathrm{AGI2}_f}(\phi) , \quad (19)$$

where R_{AGI1_f} and R_{AGI2_f} are the filtered readings of

the two orthogonal tilt sensors, and the tilt-correction coefficents r_1 and r_2 were computed by analyzing data taken with deliberately imposed tilts of about 45 μrad (see Sec. IV F 3 below).

The filtered data were then cut into segments containing exactly 3 complete rotation cycles (typically 972 data points) always starting at the same torsional and rotational phase, and 6 successive data points were averaged together to simplify the subsequent analysis. The averaged, filtered data $\langle\bar{\theta}(\phi)\rangle$ were fitted to a function

$$\langle\bar{\theta}(\phi)\rangle = \sum_{n=\text{odd}} \left(c_n^{\sin}\sin n\phi + c_n^{\cos}\cos n\phi\right) + \sum_{m=0}^{2} b_m P_m(\phi) \ , \tag{20}$$

where the $c_n^{\sin}$ and $c_n^{\cos}$ coefficients account for harmonic angular deflections of the pendulum and P_m is a polynomial that accounts for residual fiber drift. The first sum runs over n=1, 3, 5, and 7 because our filter suppresses all even harmonics; the $n = 1$ terms are our signal and the remaining odd n terms provide information on gravity gradients, on turntable irregularities, and on pendulum misalignment as discussed in Sec. II E 1. Fewer than 1% of the data points were rejected in the fitting process on the basis of excess noise. The $c_n^{\sin}$ and $c_n^{\cos}$ coefficients were then corrected for attenuation and phase shift introduced by the pendulum inertia, electronic time constants, the digital filters, and the averaging process.

Each experimental *state* (a given configuration of the composition dipole on the tray and of the pendulum tray and fiber with respect to the turntable) contained about 30 three-cycle segments. The *cumulative* 1ω signal for a given *state* (denoted as $\bar{c}_1^{\sin}$ and $\bar{c}_1^{\cos}$ coefficients) was obtained as follows. We combined the $c_1^{\sin}$ and $c_1^{\cos}$ coefficients of individual segments in two different ways: weighting all points equally and weighting the points by the inverse square of the fit errors. These two analyses always gave consistent results. The central values of $\bar{c}_1^{\sin}$ and $\bar{c}_1^{\cos}$ were taken as the average of the two means and the uncertainties as the larger of the two errors (which was usually the error from the unweighted analysis).

The central values from the various *states* were combined to extract the UFF-violating signal as follows. We first calculated the instrumental offset O by averaging the 1ω signals observed in the N individual *data sets*, where each data set was characterized by a definite experimental *state*:

$$O^{\sin} = \frac{1}{N}\sum_{j=1}^{N}(\bar{c}_1^{\sin})_j, \quad O^{\cos} = \frac{1}{N}\sum_{j=1}^{N}(\bar{c}_1^{\sin})_j \ . \tag{21}$$

The offset contained no contribution from a UFF-violating interaction because its effects canceled when summed over a complete set of *states*. We then found the deviations D_j of the 1ω signals in each *state* from the offset O,

$$D_j^{\sin} = (\bar{c}_1^{\sin})_j - O^{\sin}, \quad D_j^{\cos} = (\bar{c}_1^{\cos})_j - O^{\cos} \ . \tag{22}$$

Next we rotated these derivations so they would add coherently if they arose from an external torque on the composition dipole,

$$\begin{aligned} \tilde{D}_j^{\sin} &= +D_j^{\sin}\cos\delta + D_j^{\cos}\sin\delta \ , \\ \tilde{D}_j^{\cos} &= -D_j^{\sin}\sin\delta + D_j^{\cos}\cos\delta \ , \end{aligned} \tag{23}$$

where δ is defined in Eq. (7). Our UFF-violating signal S_{UFF} was then the average of the $\tilde{D}_j$'s and the error δS_{UFF} was determined by the scatter of the points,

$$S_{\text{UFF}}^{\sin} = \frac{1}{N}\sum_{j=1}^{N}\tilde{D}_j^{\sin}, \quad S_{\text{UFF}}^{\cos} = \frac{1}{N}\sum_{j=1}^{N}\tilde{D}_j^{\cos} \ , \tag{24}$$

$$\delta S_{\text{UFF}}^{\sin} = \sqrt{\frac{1}{N}\sum_{j=1}^{N}\frac{(\tilde{D}_j^{\sin} - S_{\text{UFF}}^{\sin})^2}{N-2}}, \quad \delta S_{\text{UFF}}^{\cos} = \sqrt{\frac{1}{N}\sum_{j=1}^{N}\frac{(\tilde{D}_j^{\cos} - S_{\text{UFF}}^{\cos})^2}{N-2}} \ .$$

In one case the δS_{UFF} error was slightly smaller than the uncertainty one would obtain by propagating the errors in the $\bar{c}_1^{\sin}$ and $\bar{c}_1^{\cos}$ coefficients; for that one case we used the propagated (larger) error.

For diagnostic purposes we repeated the procedure given in Eqs. (21)–(24) and extracted the corresponding offsets $O_n^{\sin}$ and $O_n^{\cos}$ and "signals" $S_n^{\sin}$ and $S_n^{\cos}$ associated with the $\bar{c}_n^{\sin}$ and $\bar{c}_n^{\cos}$ coefficients with $n = 3$, 5, and 7.

B. Analysis of differential accelerations toward astronomical sources

We extracted differential acceleration signals toward astronomical sources by taking advantage of the fact that essentially all of our systematic effects were fixed in the laboratory frame. We therefore chose to look for the sidereal (or solar) daily modulation of the $c_1^{\sin}$ and $c_1^{\cos}$ coefficients caused by the movement of the astronomical sources in Earth's frame. A UFF-violating signal from any astronomical source that is not in Earth's equatorial plane also has a constant component lying in the north-south direction, but we ignored this constant component as it may be contaminated by systematic effects fixed in the laboratory frame.

We began our analysis by dividing the $\bar{\theta}(\phi)$ data for each test-body pair into segments containing precisely two complete rotations of the turntable, during which time the sources had typically moved by only 52°. We extracted the $c_1^{\sin}$ and $c_1^{\cos}$ coefficients for each segment as described above, and computed the altitude ϑ and az-

imuth φ of the source at the effective midpoint of each data segment, approximating the Sun and Galaxy as sources that remained stationary during a segment. Our results were later corrected for the ≈5% attenuation introduced by this approximation. A set of $c_1^{\sin}$ and $c_1^{\cos}$ coefficients from about 1 week of continuous data accumulation in a given *state* was then fitted by

$$\begin{aligned} c_1^{\sin}(i) &= k\cos(\vartheta_i)[-\cos(\varphi_i-\phi_0)\Delta a-\sin(\varphi_i-\phi_0)\Delta a^*] \\ &\quad +d^{\sin}, \\ c_1^{\cos}(i) &= k\cos(\vartheta_i)[+\sin(\varphi_i-\phi_0)\Delta a-\cos(\varphi_i-\phi_0)\Delta a^*] \\ &\quad +d^{\cos}, \end{aligned} \tag{25}$$

where i refers to a particular data segment, $k = 1.19\times 10^3$ rad s^2/cm is a property of our torsion pendulum, Δa is the differential acceleration toward the astronomical source, Δa^* is a quadrature acceleration that is expected to vanish within the errors of the measurement, ϕ_0 specifies the orientation of the composition dipole when $\phi = 0$, and the constants $d^{\sin}$ and $d^{\cos}$ account for effects fixed in the laboratory frame. The various $c_1^{\sin}(i)$ and $c_1^{\cos}(i)$ coefficients were weighted equally in the fitting process. Our quoted values of Δa and Δa^* for a given test-body pair were found by combining the individual fit values weighted by the inverse square of their errors.

IV. EXPERIMENTAL RESULTS

A. Data aquisition protocol

We followed a standard procedure each time the test-body configurations were changed. After installing the test bodies and evacuating the chamber to 2×10^{-2} Torr, we measured the pendulum $\bar{q}_{21}$ by taking data with the Q_{21} compensator reversed. If the observed signal exceeded 200 nrad, we opened the apparatus, adjusted the trim screws to reduce $\bar{q}_{21}$, and began again. One iteration usually sufficed. (This tuning procedure, of course, was only used after the trim screws were installed early in 1993.) The apparatus was then heated to 50 °C for 24 h and cooled back to the normal operating temperature of 23.5 °C. This procedure reduced the fiber drift rate to $\leq$ 4 μrad/h. The Q_{21} compensator was then returned to its normal position, and a dynamic calibration (see Sec. IV E below) was made. Next a series of tilt-calibration runs were taken to determine the tilt matrix (see Sec. IV F 3). Then UFF data were taken over a period of 7–9 days. At the midpoint of the UFF data accumulation, we made magnetic systematic tests and measured the $\bar{q}_{31}$ and $\bar{q}_{41}$ moments of the pendulum. After the UFF data were obtained, we modulated the temperature of the thermal shields by ±1.1 °C. Finally, we repeated the dynamic calibration to test the stability of the instrument.

We used a simpler procedure in the Si/Al-Cu experiment as we were not studying differential acceleration in Earth's field and therefore did not need to control gravity gradients so carefully. We kept the test bodies in a single configuration and simply rotated the top fiber attachment to take data with each of the four mirrors in the autocollimator beam; this obviated the need to open the apparatus after it was initially heated and cooled down. Before beginning an UFF data run we made a dynamic calibration and completed a series of tilt-calibration runs. After taking UFF data for a period of about 7 days we rotated the fiber to a new mirror and began with a new dynamic calibration.

B. Data with a Be-Al dipole

These data were taken between December 1991 and April 1992 with the pendulum shown in the left of Fig. 2. The turntable rotation period τ_c was set to $\tau_c = 9\tau_0 = 6231.2$ s. A total of 205 three-cycle data segments were acquired in 4 different *states*. Data taken in each *state* were divided into three sets: one containing data taken before the systematic error tests performed at the midpoint of the data taking sequence, one containing data taken after the tests, and one containing the average of the $\bar{q}_{31}$ measurements (because the applied Q_{31} was reversed during these tests, there was no net contribution from the applied Q_{31} fields). The data were divided in this way so that a meaningful error could be extracted from the scatter of a significant number ($N = 12$) of data sets.

C. Data with a Be-Cu dipole

These data were taken between April 1992 and July 1992 with the pendulum shown in the left of Fig. 2 and the turntable rotating in the reverse direction with $\tau_c = 9\tau_0$ or $\tau_c = 8\tau_0$ (labeled Be-Cu I), and between January 1993 and May 1993 with the pendulum shown in the right of Fig. 2 and the turntable rotating normally with a period $\tau_c = 9\tau_0$ (Be-Cu II). A total of 479 three-cycle data segments were acquired in 8 different *states*. Equations (21)–(23) were used 3 times for these data: once for Be-Cu I data with $\tau_c = 9\tau_0$ ($N = 6$), once for the Be-Cu I data with $\tau_c = 8\tau_0$ ($N = 6$), and once for the Be-Cu II data ($N = 12$). The 24 $D_j^{\sin}$'s and 24 $D_j^{\cos}$'s were combined using Eq. (24) with the factor $N-2$ replaced by $N-4$.

D. Data with a Si/Al-Cu dipole

These data were taken between May 1993 and September 1993 with the pendulum shown in the right of Fig. 2. The turntable rotation period τ_c was set to $\tau_c = 9\tau_0$. In this case we were interested in obtaining the acceleration toward astronomical sources (especially the Sun), and so the experimental *states* were selected to give optimum sensitivity for a signal modulated in the laboratory frame. Therefore, we did not interchange the test bodies on the pendulum tray to cancel the effects of laboratory-fixed gravity gradients coupling to distortions of the pendu-

lum tray. Instead, we took data on all four mirrors of the pendulum, because rotating the pendulum to a different mirror could be done rapidly and with little disturbance to the rest of the apparatus.

E. Calibrations

As our methods for calibrating κ and θ, the torsional constant of the fiber and the angular deflection, are described in Ref. [11] we present here only the results.

During the course of this work we regularly made *dynamic* calibrations by observing the pendulum response to an abrupt, well-known change in the turntable speed. These could be done rapidly and with good precision. A typical result is shown in Fig. 10. These data determined the angular deflection scale, the free-oscillation period τ_0, and damping time τ_d. Because the pendulum moment of inertia could be calculated reliably, the measurement of τ_0 also determined the fiber constant κ. The values of κ were found to be very stable and yielded $\kappa = (0.0330 \pm 0.0005)$ erg/rad, where the error is dominated by uncertainties in the calculated moment of inertia.

We also made two *gravitational* calibrations of our instrument by installing Q_{44} sources and observing the 4ω signals induced by their coupling to the known (see Table IV) $\bar{q}_{44}$ moment of the pendulum. The first test, shown in Fig. 14, used four 486 g masses placed at 90° intervals 35.5 ± 0.1 cm from the torsion pendulum to create a hexadecapole field of $Q_{44} = (1.91 \pm 0.02) \times 10^{-5} \mathrm{g/cm^5}$. The resulting 4ω amplitude 428 ± 16 nrad and phase $44.0 \pm 0.6°$ agreed with the 439 ± 6 nrad and 45.0° values predicted from the calculated $\bar{q}_{44}$ and Q_{44} moments, and the measured κ.

The second test used a much weaker Q_{44} source to check that we could correctly detect a very small signal. This source consisted of four 32.5 g masses placed symmetrically around the balance at a distance of 32.2 cm to give $Q_{44} = (1.66 \pm 0.02) \times 10^{-6}$ g/cm^5. The results of this test are shown in Fig. 15. The observed 4ω amplitude and phase, 44 ± 8 nrad and $(45 \pm 3)°$, agreed well with the expected values of 38.0 ± 0.4 nrad and 45°. The induced torque in this case was equivalent to a UFF violation of $\eta = 2.1 \times 10^{-11}$ (a value consistent with the null results of Ref. [1]) in our normal mode of operation.

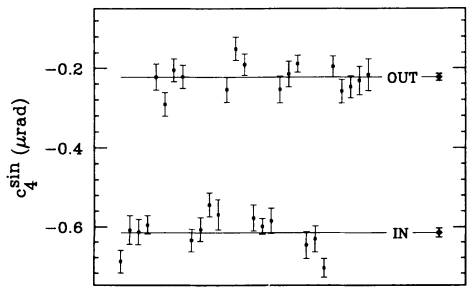

FIG. 14. Direct gravitational calibration using a known Q_{44} source. The source was installed and removed four times to discriminate against the small background Q_{44} gradient. The observed 4ω signal of 428 ± 16 nrad agreed well with the 439 ± 6 nrad value predicted from the dynamic calibration.

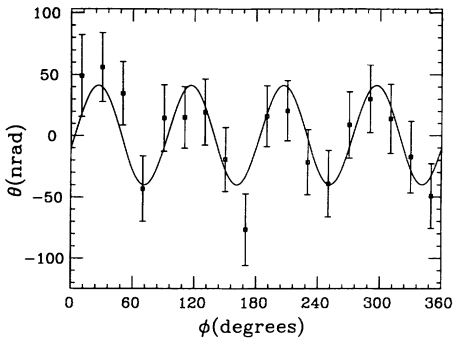

FIG. 15. Demonstration of our experimental sensitivity using a Q_{44} source that generated a 4ω signal of the same amplitude as the 1ω signal produced by a UFF-violating interaction with $\eta = 2.1 \times 10^{-11}$. This plot was made by subtracting source-out data from source-in data and binning the results in ϕ. Fiber drift has been subtracted. The best-fit 4ω signal (shown as a solid curve) has an amplitude and phase, (44 ± 8) nrad and $(45 \pm 3)°$, in excellent agreement with the expected values of 38 nrad and 45°, respectively.

F. Systematic effects

Our strategy for treating systematic effects was described in Ref. [11]. We identified the various "driving terms" that could induce systematic errors, measured these driving terms during the course of the normal data-taking, and then in subsidiary measurements deliberately induced such "driving terms" with amplitudes large enough to produce detectable signals. These subsidiary measurements yielded the sensitivity to the "driving terms" and allowed us either to make corrections (with associated uncertainties) or to place upper limits on their contribution to the systematic errors. Such systematic tests occupied a significant fraction of our total effort.

The results of the systematic tests are summarized in Table V. The most important systematic effects were

TABLE V. Systematic error budget for the angular deflection signal (in nrad).

Effect	Be-Al	Be-Cu
Q_{21} gradient	1.1	0.7
Q_{31} gradient	1.3	0.8
Q_{41} gradient	0.5	0.4
$l > 4$ gradients	0.2	0.2
Linear tilt	0.1	0.2
Magnetism	0.05	0.1
Thermal 1ω	0.4	0.4
Thermal gradient	0.07	0.07
Calibration drifts	0.4	0.4
Total	1.9	1.3

gravity gradients, tilt of the rotation axis, and irregularities in the turntable rotation rate.

1. *Gravity gradients*

The systematic uncertainties from gravity gradients were derived from Eq. (13) using the measured values or limits of $\bar{q}_{l1}$ and Q_{l1}. Because the largest local gradient field Q_{21} was found to change with time (see Sec. II E 5), the Q_{21} gradient was measured before and after each set of UFF measurements in a given *state*. If the gradient was found to have changed, lead bricks were added or removed from the floor to maintain Q_{21} to below 0.015 g/cm^3, the value used to assign the associated systematic error. The component of $\bar{q}_{21}$ correlated with the composition dipole of the pendulum was used to assign the systematic error. No corrections to the data were made for the $q_{21}Q_{21}$ coupling.

The Q_{31} field at the pendulum was measured using the $\bar{q}_{31}$ gradiometer shown in Fig. 6. Small lead bricks were then mounted on the thermal shield to reduce this field by a factor of 8 (see Table III). The residual Q_{31} field did not vary with time; the variation expected from the rain water was much smaller than our errors. A fraction of the data in each *state* was taken with a large applied Q_{31} field that pointed first to one side and then to the opposite side of the apparatus. The difference between the signals in these two cases measured the $\bar{q}_{31}$ moment of the pendulum. For the Be-Al and Be-Cu I data, we observed a nonzero $\bar{q}_{31}$ moment that was largely independent of the orientation of the composition dipole (we attributed this moment to the known $\bar{q}_{30}$ moment of the pendulum accompanied by a permanent pendulum "tip" of ≈ 1 mrad) and applied $q_{31}Q_{31}$ corrections of around 5 nrad to each *state* of the Be-Al and Be-Cu I data. When the compensating screws were added to the pendulum countermasses, we reduced the $\bar{q}_{30}$ moment by a factor of 7. After this change was made, the $\bar{q}_{31}$ moment was no longer resolved and $q_{31}Q_{31}$ corrections to the Be-Cu II and Si/Al-Cu data were not required. The uncertainties in our measurements of the $q_{31}Q_{31}$ coupling lead to the systematic error in Table V.

Although the Q_{21} compensator masses were designed to minimize the accompanying Q_{41} field, $\bar{q}_{41}$ gradiometer measurements revealed a small Q_{41} field that rotated with the Q_{21} compensator masses, and a negligible Q_{41} field fixed in the laboratory frame. After the Be-Cu I data were taken, the Q_{21} compensators were modified to reduce their residual Q_{41} field as indicated in Table III. Test-body imperfections or a pendulum "tip" that changed as the test bodies were moved between *states* could give the pendulum a q_{41} moment that tracked the composition dipole. By measuring the $q_{22}Q_{22}$ and $q_{21}Q_{21}$ couplings and comparing the torsional periods (and hence moments of inertia) in different *states*, we demonstrated that the test bodies were located on the pendulum tray with a reproduceability of better than 2×10^{-3} cm. A test body displaced by this amount would change the pendulum "tip" by less than 0.1 mrad; if this "tip" followed the composition dipole, it would give a systematic error of 0.1 nrad. Test-body imperfections gave a larger $q_{41}Q_{41}$ error. The measured *state*-to-*state* variation of q_{21} indicated that the test-body centers of mass were not exactly coplanar. The inferred displacement of the centers of mass corresponded to a q_{41} moment of less than 1.0 g cm^4, leading to the systematic error given in Table V.

We calculated the Q_{51} and Q_{61} fields produced by our local Q_{31} and Q_{21} compensator masses. (Because these higher multipole fields were not made small by design, the calculations are reliable at the few percent level.) The pendulum had a small, calculable $\bar{q}_{51}$ moment because the individual test bodies did not have identical q_{40} moments, and could acquire $\bar{q}_{51}$ and $\bar{q}_{61}$ moments through test body imperfections or "tip." Considerations similar to those given above for $\bar{q}_{41}$ led to systematic errors from these higher multipole orders at or below the 0.2 nrad level.

2. *Turntable irregularities*

Reproducible turntable imperfections create deviations from a constant rotation rate that are essentially periodic at a harmonic of the rotation frequency [13], $\omega_c = 2\pi/T_c$, where T_c is the turntable rotation period. If the departure from a constant rotation rate is expanded in a Fourier series,

$$\omega(t) = \omega_c + \sum_{n=1}^{N} w_n e^{-in\omega_c t} , \tag{26}$$

then the response of the torsion balance will be

$$\theta(t) = \sum_{n=1}^{N} \frac{-in\omega_c}{\omega_0^2 - (n\omega_c)^2} w_n e^{-in\omega_c t} , \tag{27}$$

where pendulum damping has been neglected, and ω_0 is the torsional frequency (typically, $\omega_0 = 9\omega_c$). The $n = 1$ term will generate an offset O, but will not be mistaken for a UFF-violating signal because it is independent of the orientation of the composition dipole. It is interesting to note from Table VI that the 3ω, 5ω, and 7ω offsets are nonzero and comparable in magnitude to the 1ω offset, while the components that track the composition dipole vanish. Because we know of no other mechanism that would produce 3ω, 5ω, and 7ω offsets, we attribute these to a periodic kick in the turntable rotation rate (a square wave kick would give roughly equal amplitudes for the 1ω, 3ω, 5ω, and 7ω offsets). The presence of these higher harmonic offsets leads us to conclude that the 1ω offset arose from a turntable irregularity.

If w_1 fluctuates in time, it will produce excess noise in our 1ω coefficients. The effects of such *nonreproducible* or slowly drifting irregularities are included in the statistical errors defined in Eq. (24).

TABLE VI. Signals and offsets (in nrad) in our measurements of differential accelerations in the field of Earth. The Be-Cu I data are not shown because they were taken at two different speeds which could have had different offsets.

Test-body pair	n	$S_n^{\sin}$	$S_n^{\cos}$	$O_n^{\sin}$	$O_n^{\cos}$
Be-Al	1	-1.1 ± 5.2	-2.5 ± 5.0	-14.6 ± 5.3	-56.4 ± 5.7
	3	-4.5 ± 8.0	9.5 ± 7.4	-30.8 ± 5.8	43.2 ± 9.2
	5	5.7 ± 7.3	5.0 ± 8.2	38.3 ± 9.5	41.3 ± 5.1
	7	1.1 ± 7.0	2.2 ± 7.2	-22.3 ± 8.4	10.5 ± 4.7
Be-Cu II	1	-1.6 ± 6.9	-10.7 ± 7.4	-10.7 ± 8.6	-76.5 ± 5.4
	3	-0.9 ± 6.5	3.5 ± 7.0	-36.8 ± 7.4	-0.8 ± 5.0
	5	-3.1 ± 7.7	0.4 ± 8.7	17.5 ± 8.1	46.4 ± 7.3
	7	-6.3 ± 4.4	-0.3 ± 4.2	-2.3 ± 3.9	21.1 ± 4.7

3. Tilt

Tilt was continuously monitored by two orthogonal electronic level sensors mounted near the autocollimator. The 1ω signals from these two sensors AGI1 and AGI2 were analyzed to yield the base plate tilt, i.e., the deviation between the turntable axis and local vertical as defined by the freely hanging torsion fiber, and showed that the tilt of our laboratory floor changes by as much as several μrad per day. During normal data acquisition, the apparatus was releveled once each day so that the tilt was less than 1 μrad. The rotating level sensors also showed a 5 μrad amplitude 2ω signal, very constant in time, that corresponded to a wobble of the rotation axis at the turntable rotation frequency.

We determined the sensitivity of the autocollimator signal to tilt by deliberately tilting the turntable baseplate by ± 45 μrad about two orthogonal axes and measuring the induced 1ω signal from the autocollimator. A set of such "tilt calibration" runs overdetermined the "tilt matrix" $\mathbf{M}$ defined by

$$\begin{pmatrix} \Delta c_1^{\sin} \\ \Delta c_1^{\cos} \end{pmatrix} = \begin{pmatrix} M\cos\psi & M\sin\psi \\ -M\sin\psi & M\cos\psi \end{pmatrix} \begin{pmatrix} t_x \\ t_y \end{pmatrix}, \quad (28)$$

where $\Delta c_1^{\sin}$ and $\Delta c_1^{\cos}$ are the induced 1ω signals from the autocollimator, M and ψ are two parameters that determine $\mathbf{M}$, and t_x and t_y are the orthogonal components of the base plate tilt.

We found that M was about 0.05. By comparing the tilt matrices for runs in which the autocollimator viewed each of the four mirrors on the pendulum, we discovered that the tilt sensitivity arose in the upper fiber attachment. Table VII shows that as the upper fiber attachment is rotated inside the apparatus by angles of 90°, 180°, and 270°, the phase of $\mathbf{M}$ rotates correspondingly, while the magnitude of $\mathbf{M}$ is nearly constant. (We ascribe the small variation in M to a slight misalignment of the upper fiber attachment mechanism.) Auxiliary measurements showed that the tilt systematic was linear, i.e., that $\mathbf{M}$ was independent of the magnitude of the deliberately induced baseplate tilt.

Our data were then corrected for the instantaneous tilt using Eq. (19), where the coefficients r_1 and r_2 were computed from the measured value of $\mathbf{M}$. This procedure had the advantage that it corrected properly (to the extent that the tilt effects are frequency independent) for all kinds of level variations including wobble, and not just base plate tilt. We verified that this tilt-correction procedure was valid by analyzing correlations of the 1ω θ, AGI1, and AGI2 signals for all the nominally level runs of a given *state*. Before the tilt correction was applied, θ and AGI1 and AGI2 were highly correlated with correlation coefficients of ≈ 0.60 (for 36 runs). After the tilt correction, the correlation coefficients were reduced to ≈ 0.18, consistent with uncorrelated populations.

The error from the tilt correction procedure, shown in Table V, was derived by multiplying the uncertainties in r_1 and r_2 by the average tilt of the runs in each *state*.

TABLE VII. Tilt matrix measured on four different mirrors. As the upper fiber attachment was rotated to the different values of ϕ_{top}, the angle ψ of the tilt matrix rotated correspondingly while the magnitude of the tilt matrix, M, was approximately constant. This demonstrated that the sensitivity to tilt arose in the upper fiber attachment.

ϕ_{top}	M	ψ	$\phi_{\text{top}} - \psi$
0°	$(5.10 \pm 0.06) \times 10^{-2}$	$(-105.8 \pm 0.7)°$	$(105.8 \pm 0.7)°$
90°	$(4.43 \pm 0.04) \times 10^{-2}$	$(-18.0 \pm 0.6)°$	$(108.0 \pm 0.6)°$
180°	$(5.21 \pm 0.07) \times 10^{-2}$	$(73.5 \pm 0.8)°$	$(106.5 \pm 0.8)°$
270°	$(5.75 \pm 0.06) \times 10^{-2}$	$(173.7 \pm 0.6)°$	$(96.7 \pm 0.6)°$

4. Magnetic effects

We determined the magnetic moments of our pendulums by removing the three-layer magnetic shielding, turning off the three-axis Helmholtz coils, and measuring the 1ω autocollimator signal in the ambient (≈ 300 mG) field of the laboratory for two mirror-image configurations (A and B) of the test bodies on the pendulum tray. The difference between the 1ω signals, $(A_{1\omega}^M - B_{1\omega}^M)/2$, measured the test-body magnetic dipole moment, while

TABLE VIII. Tests for magnetic effects, showing the 1ω signals (in μrad) measured with the magnetic shields removed and the Helmholtz coils off.

Pendulum	$[A_{1\omega}^M + B_{1\omega}^M]/2$	$[A_{1\omega}^M - B_{1\omega}^M]/2$
Be-Al	255.12 ± 0.17	4.59 ± 0.17
Be-Cu I	254.52 ± 0.15	4.94 ± 0.15
Be-Cu II	9.51 ± 0.05	5.38 ± 0.05
Si/Al-Cu	11.37 ± 0.05	0.64 ± 0.05

$(A^M_{1\omega} + B^M_{1\omega})/2$ measured the dipole moment of the pendulum tray. The results of these measurements are shown in Table VIII.

The sensitivity of our balance to a pendulum magnetic moment depends on two factors—the cancellation factor f_{HH} of the Helmholtz coils and the attenuation factor $f_{\rm mag}$ of the three-layer magnetic shields. These were deduced from the Be-Al and Be-Cu I measurements for which the tray had a dipole moment 50 times larger than the test bodies. We found that $f_{HH} = 28$ by removing the two innermost magnetic shields and comparing the 1ω signals with the coils on and off. We obtained $f_{\rm mag} > 3600$ by turning off the Helmholtz coils and comparing the 1ω signals with all shields removed (255 μrad) to that with the shields in place (< 70 nrad). The magnetic systematic error listed in Table V is $(A^M_{1\omega} - B^M_{1\omega})/(2f_{HH}f_{\rm mag})$.

After the pendulum compensator masses were replaced to provide adjustment screws, the pendulum's dipole moment diminished by a factor of 25; apparently one of the original compensator masses contained a ferromagnetic impurity.

5. *Thermal effects*

Temperature modulation at the turntable rotation frequency could create a spurious 1ω autocollimator signal because the fiber drift rate was a strong function of temperature. We measured the sensitivity of the torsion balance to temperature fluctuations by modulating at 1ω the constant-temperature baths by ± 1.1 K; this induced a 2.4 μrad 1ω signal on the torsion balance. During normal data acquisition, the largest 1ω variation of any of the eight temperature sensors on the apparatus was 0.15 mK. Because the most likely sources of temperature variations were fluctuations in the power dissipated in the turntable drive and fluctations of the temperature of the thermal shield, we based our thermal-variation systematic error on the temperature sensor mounted on the outer thermal shield close to the turntable motor; this sensor showed 1ω variations of < 0.12 mK in normal runs and 900 mK in the temperature-modulated runs. We assigned an error of 0.15 mK/900 mK$\times$2.4 μrad = 0.4 nrad, where, to be conservative, we used the largest observed 1ω variation rather than the < 0.12 mK value from the sensor closest to the motor.

We were also concerned that temperature gradients across the apparatus could cause a torsion balance response and monitored these gradients by regularly interchanging temperature sensors on opposite sides of the apparatus to provide cross calibrations. In normal operation, the largest temperature difference across the heat shield was less than 20 mK, and this difference was stable to better than 3 mK in the different *states*. We found the sensitivity to temperature gradients by isolating one upper and lower heat panel of the outer thermal shield and raising their temperatures by 4.5 K relative to the rest of the thermal shield. This induced a 1ω torsional signal of less than 100 nrad. The thermal gradient systematic error was obtained from 3 mK/4.5 K $\times$ 100 nrad = 0.07 nrad.

6. *Calibration drifts*

The dynamic calibrations made several times in each experimental *state* were in very good agreement. The measured amplitudes varied by 0.3% because the torsion balance had a small random amplitude at the start of the calibration runs. The torsional period fluctuated by 0.2%, either because imperfect test-body reversals changed the moment of inertia or because κ changed as the pendulum was parked and unparked for test-body reversals. We added these two uncertainties in quadrature and multiplied by the autocollimator *offset* signal to obtain the calibration drift systematic error.

G. Results

1. *Differential acceleration in Earth's field*

The results of our analysis are summarized in Table VI. The UFF-violating signals and associated 1σ statistical errors are

$$\begin{aligned} &\text{Be-Al}: \quad S^{\rm sin}_{\rm UFF} = -1.1 \pm 5.1\,\text{nrad}, \quad S^{\rm cos}_{\rm UFF} = -2.5 \pm 5.1\,\text{nrad}\ ; \\ &\text{Be-Cu}: \quad S^{\rm sin}_{\rm UFF} = +1.0 \pm 4.7\,\text{nrad}, \quad S^{\rm cos}_{\rm UFF} = -5.6 \pm 4.7\,\text{nrad}\ , \end{aligned} \tag{29}$$

where the Be-Al and Be-Cu results come from combining 12 and 24 data sets, respectively. (The Be-Cu results have relatively larger errors because those data were taken at three different turntable speeds with three different offsets. This was not an optimum use of our running time, but was done to investigate the origin of the offset.) We obtained our final values

$$\begin{aligned} &\text{Be-Al}: \quad S^{\rm sin}_{\rm UFF} = -1.1 \pm 5.5\,\text{nrad}, \quad S^{\rm cos}_{\rm UFF} = -2.5 \pm 5.5\,\text{nrad}\ ; \\ &\text{Be-Cu}: \quad S^{\rm sin}_{\rm UFF} = +1.0 \pm 4.9\,\text{nrad}, \quad S^{\rm cos}_{\rm UFF} = -5.6 \pm 4.9\,\text{nrad}\ , \end{aligned} \tag{30}$$

by adding in quadrature the systematic errors listed in Table V. The corresponding horizontal differential accelerations are

$$\begin{aligned} \mathbf{a}^{\rm Be}_{\perp} - \mathbf{a}^{\rm Al}_{\perp} &= [(-2.3 \pm 4.6)\hat{e} + (-0.3 \pm 4.6)\hat{n})] \times 10^{-12}\ \text{cm/s}^2\ ; \\ \mathbf{a}^{\rm Be}_{\perp} - \mathbf{a}^{\rm Cu}_{\perp} &= [(-3.6 \pm 4.1)\hat{e} + (-3.2 \pm 4.1)\hat{n})] \times 10^{-12}\ \text{cm/s}^2\ , \end{aligned} \tag{31}$$

where $\hat{e}$ and $\hat{n}$ are unit vectors pointing east and north, respectively.

2. *Differential accelerations toward the Sun, the Galaxy, and the cosmic microwave dipole*

We searched for accelerations toward astronomical sources using the results reported in this paper together with the data of Ref. [11]. We first discuss our 1σ results for accelerations toward the Sun. By combining 470 two-cycle segments of Be-Al data spanning a total of 19 months, we find

$$\Delta a^{\odot}(\text{Be-Al}) = (+2.4 \pm 5.8) \times 10^{-12}\ \text{cm/s}^2\ ,$$
$$\Delta a^{*}(\text{Be-Al}) = (+2.6 \pm 5.8) \times 10^{-12}\ \text{cm/s}^2\ , \quad (32)$$

where $\Delta a^{\odot}$ and Δa^{*} point toward the Sun and 90° away from the Sun, respectively, and a positive $\Delta a^{\odot}$ indicates that the first test body (Be in this case) has the greater acceleration toward the source. From 829 two-cycle segments of Be-Cu data spanning a total of 47 months, we find

$$\Delta a^{\odot}(\text{Be-Cu}) = (-3.0 \pm 3.6) \times 10^{-12}\ \text{cm/s}^2\ ,$$
$$\Delta a^{*}(\text{Be-Cu}) = (-3.4 \pm 3.6) \times 10^{-12}\ \text{cm/s}^2\ . \quad (33)$$

From 274 two-cycle segments of Si/Al-Cu data spanning a total of 2 months, we obtain

$$\Delta a^{\odot}(\text{Si/Al-Cu}) = (+3.0 \pm 4.0) \times 10^{-12}\ \text{cm/s}^2\ ,$$
$$\Delta a^{*}(\text{Si/Al-Cu}) = (-3.0 \pm 4.0) \times 10^{-12}\ \text{cm/s}^2\ . \quad (34)$$

The corresponding differential accelerations toward the galactic center are

$$\Delta a^{\text{gal}}(\text{Be-Al}) = (+9.1 \pm 7.0) \times 10^{-12}\ \text{cm/s}^2\ ,$$
$$\Delta a^{*}(\text{Be-Al}) = (-3.8 \pm 7.0) \times 10^{-12}\ \text{cm/s}^2\ , \quad (35)$$

$$\Delta a^{\text{gal}}(\text{Be-Cu}) = (-6.7 \pm 4.5) \times 10^{-12}\ \text{cm/s}^2\ ,$$
$$\Delta a^{*}(\text{Be-Cu}) = (+4.4 \pm 4.5) \times 10^{-12}\ \text{cm/s}^2\ , \quad (36)$$

and

$$\Delta a^{\text{gal}}(\text{Si/Al-Cu}) = (+3.4 \pm 5.0) \times 10^{-12}\ \text{cm/s}^2\ ,$$
$$\Delta a^{*}(\text{Si/Al-Cu}) = (+2.8 \pm 5.0) \times 10^{-12}\ \text{cm/s}^2\ . \quad (37)$$

Our differential accelerations in the direction of the cosmic microwave background (CMB) dipole are

$$\Delta a^{\text{CMB}}(\text{Be-Al}) = (-10.9 \pm 8.8) \times 10^{-12}\ \text{cm/s}^2\ ,$$
$$\Delta a^{*}(\text{Be-Al}) = (+2.0 \pm 8.8) \times 10^{-12}\ \text{cm/s}^2\ , \quad (38)$$

$$\Delta a^{\text{CMB}}(\text{Be-Cu}) = (+9.5 \pm 5.7) \times 10^{-12}\ \text{cm/s}^2\ ,$$
$$\Delta a^{*}(\text{Be-Cu}) = (-1.8 \pm 5.7) \times 10^{-12}\ \text{cm/s}^2\ , \quad (39)$$

and

$$\Delta a^{\text{CMB}}(\text{Si/Al-Cu}) = (-2.2 \pm 6.4) \times 10^{-12}\ \text{cm/s}^2\ ,$$
$$\Delta a^{*}(\text{Si/Al-Cu}) = (-6.3 \pm 6.4) \times 10^{-12}\ \text{cm/s}^2\ . \quad (40)$$

The errors on the accelerations toward the Galaxy, and in the frame where the CMB is isotropic, are larger than those toward the Sun because the larger altitudes of these extra-solar sources attenuate their signals. We ascribe no significance to the "positive" result in Eq. (39) because one expects 1/3 of our results to lie outside the 1σ errors even if there were no UFF violation.

V. SOME IMPLICATIONS OF OUR RESULTS

A. Constraints on new Yukawa interactions

1. *Results from accelerations in Earth's field*

To set upper limits on the hypothetical Yukawa interaction specified in Eqs. (2) and (3), our limits on differential acceleration given in Eq. (31) must be combined with a calculation of the source strength defined in Eq. (5). We adopt the $\vec{J}_{\perp}(\lambda)$ for our site described in Refs. [11] and [14]. Table IX lists, for each test-body pair, our values for the product $\alpha_5 \Delta(q_5/\mu)(q_5/\mu)_S$ as a function of the range λ of the interaction. The $\alpha_5 \Delta(q_5/\mu)(q_5/\mu)_S$ values were obtained by projecting the error circle in the Δa_x, Δa_y plane onto the $\vec{J}_{\perp}(\lambda)$ axis. The "gap" in our results between $\lambda = 10$ km and $\lambda = 1000$ km occurs because it is difficult to model Earth's mass distribution with sufficient accuracy on length scales for which Earth cannot be approximated as a fluid in equilibrium under gravitational and centrifugal forces; nor can it be modeled simply in terms of the surface topography and bedrock profiles.

We estimated the uncertainties in $\vec{J}_{\perp}(\lambda)$ as follows. The calculated source strength for 1 m $\leq \lambda \leq$ 100 m was tested by using our source database to compute the Q_{21} gradient which is dominated by the distribution of nearby matter. The predicted value agreed with our measurements to within 2%; this agreement is probably fortuitous and we estimate the uncertainty in J to be 7%. We recomputed $\vec{J}_{\perp}(\lambda)$ for 100 m$\leq \lambda \leq 10^4$ m using the topography from digitized U.S. Geological Survey data, plus a model of the subsurface density distribution derived from measured surface gravity and seismic velocities. By comparing this calculation to that given in Ref. [11], we estimate uncertainties of 7%, 25%, and 30% for $\lambda = 100$ m, $\lambda = 1$ km, and $\lambda = 10$ km, respectively. For $\lambda \geq 10^6$ m, we estimate the uncertainty in $\vec{J}_{\perp}(\lambda)$ by considering the effects on our layered ellipsoidal Earth model [11,14] of ignoring the local topography. We estimate uncertainties of 20%, 2%, and $< 1\%$ for $\lambda = 10^6$ m, $\lambda = 6 \times 10^6$ m, and $\lambda => 10^7$ m, respectively.

To restrict α_5 (or equivalently $g^2/4\pi$) one needs to specify the "charge" to which the hypothetical interaction couples. We first discuss *vector* interactions because the vector "charge" of electrically neutral, stable matter is easily parametrized [see Eq. (6)]. Figure 16 shows the constraints on $\mp g^2/4\pi$ as a function of λ for the vector charges $q_5 = B$ and $q_5 \propto B - L$. This figure includes our results based on the data in Table IX, as well as those from other sensitive composition dependence [1,2,15–17]

TABLE IX. 1σ constraints[a] on macroscopic-ranged scalar or vector interactions.

λ (m)	$\alpha_5\Delta(q_5/\mu)_{\text{Be-Al}}\langle q_5/\mu\rangle_S$	$\alpha_5\Delta(q_5/\mu)_{\text{Be-Cu}}\langle q_5/\mu\rangle_S$
1	$(-1.6\pm3.6)\times10^{-7}$	$(-3.7\pm3.2)\times10^{-7}$
2	$(-0.5\pm1.2)\times10^{-7}$	$(-1.2\pm1.0)\times10^{-7}$
5	$(-1.4\pm3.7)\times10^{-8}$	$(-3.8\pm3.7)\times10^{-8}$
10	$(-0.8\pm1.9)\times10^{-8}$	$(-2.0\pm1.7)\times10^{-8}$
20	$(-0.5\pm1.1)\times10^{-8}$	$(-11\pm9.8)\times10^{-9}$
50	$(-2.6\pm5.4)\times10^{-9}$	$(-5.3\pm4.8)\times10^{-9}$
100	$(-1.6\pm3.2)\times10^{-9}$	$(-3.0\pm2.9)\times10^{-9}$
200	$(-1.0\pm2.1)\times10^{-9}$	$(-1.8\pm1.9)\times10^{-9}$
500	$(-0.7\pm1.4)\times10^{-9}$	$(-1.0\pm1.2)\times10^{-9}$
1000	$(-0.5\pm1.1)\times10^{-9}$	$(-5.9\pm9.5)\times10^{-10}$
2000	$(-3.2\pm8.2)\times10^{-10}$	$(-2.8\pm7.3)\times10^{-10}$
5000	$(-2.0\pm6.9)\times10^{-10}$	$(-0.3\pm6.1)\times10^{-10}$
10000	$(-1.3\pm7.3)\times10^{-10}$	$(1.7\pm6.5)\times10^{-10}$
2×10^4–5×10^5	not computed[b]	not computed[b]
1×10^6	$(-0.6\pm9.4)\times10^{-11}$	$(-6.5\pm8.5)\times10^{-11}$
2×10^6	$(-0.1\pm1.7)\times10^{-11}$	$(-1.1\pm1.5)\times10^{-11}$
5×10^6	$(-0.3\pm4.9)\times10^{-12}$	$(-3.4\pm4.4)\times10^{-12}$
1×10^7	$(-0.2\pm3.4)\times10^{-12}$	$(-2.3\pm3.0)\times10^{-12}$
2×10^7	$(-0.2\pm3.0)\times10^{-12}$	$(-2.1\pm2.7)\times10^{-12}$
5×10^7	$(-0.2\pm2.9)\times10^{-12}$	$(-2.0\pm2.5)\times10^{-12}$
1×10^8–∞	$(-0.2\pm2.8)\times10^{-12}$	$(-1.9\pm2.5)\times10^{-12}$

[a]The quoted errors reflect the precision of the differential acceleration measurement. The scale-factor uncertainties from the source strength calculations are discussed in the text.
[b]The Earth model discussed in Ref. [11] is not accurate enough to give a reliable source strength for these ranges.

and $1/r^2$ [18,19] tests. Figure 17 shows, for given values of λ, constraints on $\mp g^2/4\pi$ as a function of the parameter θ_5 [defined in Eq. (6)] that specifies a general vector "charge." The $\lambda=\infty$ plot incorporates additional constraints from the solar experiments of Refs. [1] and [2], while the $\lambda=100$ m plot uses the Pb-source results of Nelson, Graham, and Newman [17] to constrain $\mp g^2/4\pi$ at the θ_5 value where q_5 of Earth vanishes.

Scalar "charges" of test bodies cannot be parametrized in as simply as vector charges. Even if the elementary interaction of the scalar field with the pointlike constituents of matter is specified, the scalar "charge" of a complex

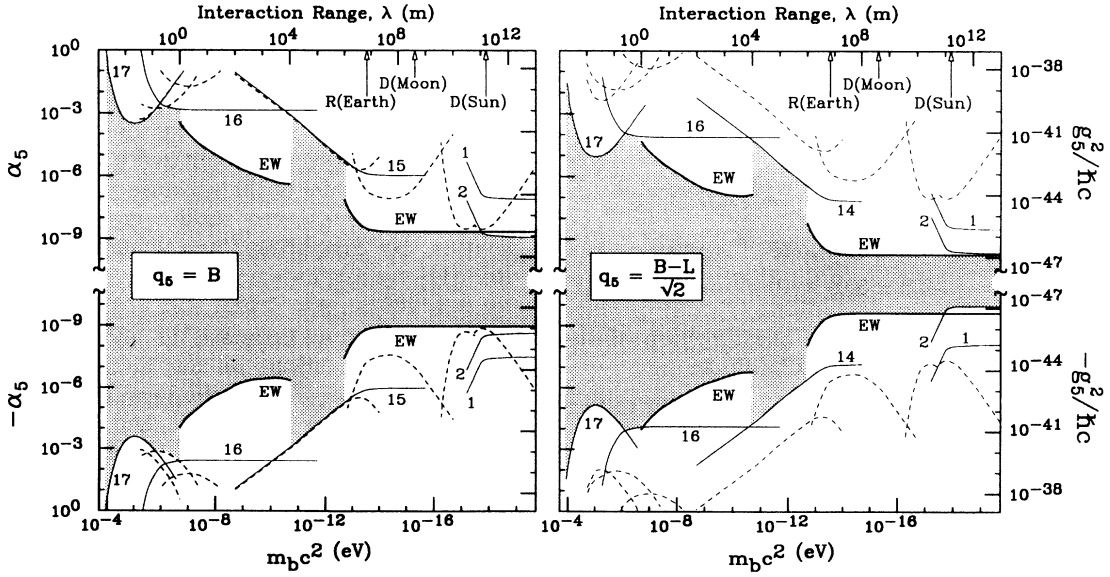

FIG. 16. 2σ upper limits on the coupling strength of a new Yukawa interaction as a function of the interaction range λ. Results are shown for possible charges of $q_5=B$ and $q_5=(B-L)/\sqrt{2}$. Heavy solid curves labeled EW are from this work. Light solid curves labeled by reference numbers are from other composition dependence and $1/r^2$ tests. Dashed curves are from tests of the $1/r^2$ law summarized in Ref. [19]. The experimentally allowed region is shaded in this and subsequent figures.

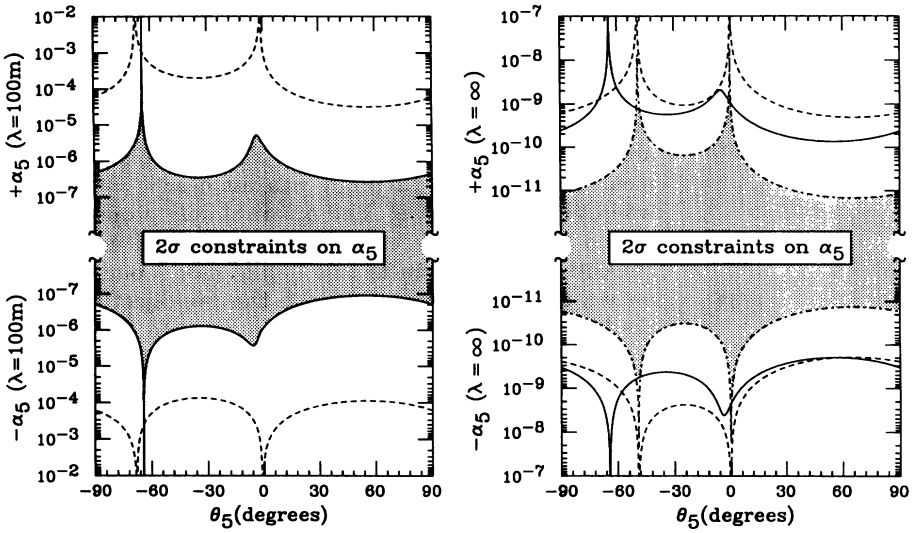

FIG. 17. 2σ upper limits on the coupling strength of a new Yukawa interaction as a function of θ_5 (a parameter that determines the vector charge of stable matter). Results are shown for two values of the range $\lambda = 100$ m and $\lambda = \infty$. The solid lines are from this work. The dashed lines in $\lambda = 100$ m plot show limits from the Pb-source experiment of Ref. [17]. The dashed and dash-dotted lines in the $\lambda = \infty$ plot are the results of the Princeton [1] and Moscow [2] experiments, respectively.

body can be found only after a detailed field-theory calculation. Although we do not here discuss any specific models of scalar fields, we have, in Table IX, given our results in a form that allows any particular scalar interaction to be tested against our data.

It is interesting to note that in string theories a scalar dilaton field arises naturally as the partner of the tensor graviton field. If this dilaton field were massless (like the graviton field), it would seem to lead to unacceptably large violations of the UFF. These effects are usually avoided by endowing the scalar field with a large mass so that it has no influence over macroscopic distances. Damour and Polyakov [4] have recently proposed a scenario containing a massless UFF-violating string-theory dilaton that tends to relax during cosmological expansion toward a state where it decouples from matter. Damour [20] estimates that at the present epoch such a scalar field would cause an UFF violation that could be as large as $\Delta a/a_g \sim 6 \times 10^{-11}$. Although a UFF violation of this magnitude is ruled out by our results, as can be seen from the last row of Table IX, the Damour-Polyakov model is consistent with much smaller effects as well and should be viewed as a motivation for improved tests of the UFF.

2. *Results for acceleration toward galactic dark matter*

There is now a large body of evidence that the accelerations of the luminous matter in our Universe are much greater than can be accounted for by the gravitational attraction of visible material. In particular, studies of the tangential accelerations of luminous matter in galaxies reveal centripetal accelerations that remain constant out to very large distances, well past the entire visible Galaxy [21,22]. These and other studies are taken as evidence that most (typically 90%) of the mass of a typical galaxy is nonluminous *dark matter* that is distributed in a large "halo" surrounding the visible Galaxy and extending far beyond the apparent galaxy. Dark matter is also invoked to explain the large-scale flows of clusters of galaxies which again substantially exceed those expected from the gravitational attractions of the luminous material. Many candidates for this dark matter have been proposed, ranging from the ordinary (normal baryonic matter in the form of nonluminous "Jupiters" [23,24]) to the exotic [25] (axions, weakly interacting massive particles, massive neutrinos, supersymmetric partners of the known particles, massive black holes, etc.).

Because of the profound nature of this observation, and because very little is known about the nature of the dark matter, it is worth performing a laboratory experiment to probe the long-range fields generated by the dark matter and make a direct test of the usual (and very reasonable) assumption that gravitation is the only significant long-range interaction between dark matter and ordinary matter [5,6]. In this section we discuss the bounds that can be placed on possible extragravitational interactions by testing the UFF for *ordinary matter* falling toward the *dark matter* in the center of our Galaxy. Upper bounds on possible nongravitational interactions between *dark matter* and *dark matter* have recently been inferred from astrophysical and cosmological considerations [26].

The acceleration of the Solar System toward the galactic center is

$$a_{\rm gal} = \omega^2 r_\odot = 1.9 \times 10^{-8}\ {\rm cm/s^2}\ , \qquad (41)$$

where $\omega = (8.4 \pm 1.0) \times 10^{-16}$ rad/s is the rotation frequency of our Galaxy and $r_\odot = 8.5 \pm 1.0$ kpc is the distance from the Sun to the galactic center. As there is ample evidence that the UFF is satisfied to high precision for ordinary matter falling toward ordinary matter [our own results in Eq. (50) indicate that $|\eta| \leq 3.0 \times 10^{-12}$] we can use our galactic results to probe the UFF for ordinary matter falling toward the dark matter in our Galaxy. To do this we need to know the fraction of $a_{\rm gal}$ that is ascribed to dark matter. Although rotation curve data suggest that about 90% of the total galactic mass is dark, the dark matter is believed to be distributed in a huge spherical halo that extends well beyond $r_\odot$. Stubbs [5] estimates that $a_{\rm gal}^{\rm DM}$, the acceleration due to the dark

matter in our Galaxy, is (25–30)% of $a_{\rm gal}$. Assuming that

$$a_{\rm gal}^{\rm DM} \approx 5 \times 10^{-9}\ {\rm cm/s^2}\ , \tag{42}$$

the results in Eqs. (35), (36), and (37) yield the following UFF tests for Be, Al, Si, and Cu falling toward dark matter:

$$\begin{aligned}\eta^{\rm DM}({\rm Be\text{-}Al}) &= (+1.8 \pm 1.4) \times 10^{-3}\ ,\\ \eta^{\rm DM}({\rm Be\text{-}Cu}) &= (-1.3 \pm 0.9) \times 10^{-3}\ ,\\ \eta^{\rm DM}({\rm Si/Al\text{-}Cu}) &= (+0.7 \pm 1.0) \times 10^{-3}\ ,\end{aligned} \tag{43}$$

where $\eta^{\rm DM} = \Delta a^{\rm gal}/a_{\rm gal}^{\rm DM}$, and the uncertainty in $a_{\rm gal}^{\rm DM}$ is not included because we do not know how to evaluate it.

For cosmological purposes we need the *total* nongravitational acceleration due to dark matter. But the results in Eqs. (43) set limits on the *differential* contribution of nongravitational interactions. If we separate the acceleration of ordinary matter due to dark matter into its gravitational and nongravitational (i.e., UFF-violating) components, $a_{\rm gal}^{DM} = a_g^{\rm DM} + a_{\rm ng}^{\rm DM}$, then for an infinite-ranged nongravitational interaction of the form specified in Eq. (3), we have

$$\frac{a_{\rm ng}^{\rm DM}}{a_{\rm gal}^{\rm DM}} = \eta^{\rm DM}\frac{\langle q_5/m\rangle}{\Delta(q_5/m)}\ , \tag{44}$$

where $\langle q_5/m\rangle$ is the average of the two test-body q_5-to-mass ratios and $\Delta(q_5/m)$ is their difference. Equation (44), when combined with the values in Eq. (43), is our *basic experimental constraint*. To proceed farther, one must evaluate the quantity

$$R = \frac{\langle q_5/m\rangle}{\Delta(q_5/m)} \tag{45}$$

for our three detector test-body pairs.

A UFF-violating interaction could arise from the exchange of scalar or vector bosons. However, as discussed in Ref. [6], a significant *vector* interaction between dark and ordinary matter is already excluded by conventional Eötvös experiments plus the requirement that the dark matter halos be stable against the repulsive vector dark-matter–dark-matter interaction. *Scalar* interactions, which would produce an attractive dark-matter–dark-matter force, are not ruled out by this argument, but can be constrained by our results in Eq. (43) and the relations given in Eqs. (44) and (45). There is no simple way to evaluate R for a general scalar interaction as it would require a detailed calculation using specific models. So we estimate R using a tree-level approximation for the scalar charge of an atom with mass number A and atomic number Z,

$$q_5(A,Z) \approx (q_5^e + q_5^p)Z + q_5^n(A-Z)\ , \tag{46}$$

where q_5^e, q_5^p, and q_5^n are the scalar charges of free electrons, protons, and neutrons, respectively. Then

$$R = \frac{\sin\psi\langle Z/m\rangle + \cos\psi\langle A/m\rangle}{\sin\psi[\Delta(Z/m)]\cos\psi[\Delta(A/m)]}\ , \tag{47}$$

where $\psi = \arctan([q_5^e + q_5^p - q_5^n]/q_5^n)$ can range, depending on the nature of the scalar interaction, from $-90°$ to $+90°$. Our constraints on the nongravitational acceleration of neutral hydrogen toward the dark matter in our Galaxy, assuming the expression for R given above, are shown as a function of ψ in Fig. 18. The experimental constraint is naturally weakest near $\psi = -0.05°$, where the charges q_5^e, q_5^p, and q_5^n are simply proportional to the masses of free electrons, protons, and neutrons, respectively. But even in this "worst case," our experimental sensitivity is good enough that we reject by 2.5σ the hypothesis that our acceleration ascribed to galactic dark matter has a nongravitational origin. We take this opportunity to note that Fig. 2 of Ref. [6], which is superceded by this work, contains an error that was traced to an incorrect sign in Ref. [31] of $\Delta B/\mu$ for a Be-Cu dipole.

Nordtvedt [27] has recently pointed out that lunar laser-ranging results provide a strong constraint on the differential acceleration of Earth and the Moon toward the galactic center. He estimates that the accumulated ranging results yield $|\Delta a| \le 10^{-13}$ cm/s^2 for this particular pair of "test bodies." Referring to Fig. 18, we note that this individual datum does not greatly improve the "worst case" upper limit on the nongravitational acceleration of neutral hydrogen toward dark matter because the "pole" for the Earth-Moon test-body pair falls near $\psi \approx 0$ where our own results are least sensitive.

We obtain a different and potentially interesting constraint by considering larger structures where dark matter appears to account for a greater fraction of our acceleration than in the case of our motion toward the galactic center. Our local group of galaxies is moving at about 600 km/s with respect to the frame in which the cosmic microwave background (CMB) is isotropic [28,29]. We estimate the corresponding accleration by dividing this peculiar velocity by the Hubble time $t_H = 1/H_0$, where $H_0 \approx 85$ km s^{-1} Mpc^{-1} [30], to obtain $a_{\rm CMB} =$

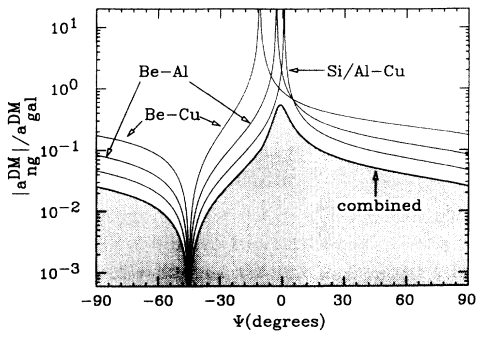

FIG. 18. 1σ constraints on the nongravitational acceleration of neutral hydrogen due to a hypothetical long-range scalar interaction with dark matter. These results are based on our data with Be, Al, Cu, and Si/Al test bodies and assume that R has the form given in Eq. (45). The vertical axis shows the ratio of the anomalous acceleration $|a_{\rm ng}^{\rm DM}|$ to the total $a_{\rm gal}^{\rm DM}$. The variable on the horizontal axis specifies the scalar charge of ordinary matter.

1.7×10^{-10} cm/s^2. This permits a crude UFF test for laboratory objects falling in the direction of the CMB dipole,

$$\eta^{\rm CMB}(\text{Be-Al}) = (-6.4 \pm 5.2) \times 10^{-2} ,$$
$$\eta^{\rm CMB}(\text{Be-Cu}) = (+5.6 \pm 3.4) \times 10^{-2} ,$$
$$\eta^{\rm CMB}(\text{Si/Al-Cu}) = (-1.3 \pm 3.8) \times 10^{-2} , \quad (48)$$

where $\eta^{\rm CMB} = \Delta a^{\rm CMB}/a_{\rm CMB}$. Although the precision of this test is not good enough to be very significant (one expects that exotic forces would lead to η's on the order of the test-body binding-energy differences which are at the part per thousand level), a hundredfold more sensitive measurement would probe the dark matter that is dominant on very large length scales—dark matter that may be different from that which is believed to dominate the mass of galaxies.

B. Equivalence principle

The differential acceleration limits given in Eq. (31) imply 1σ limits on violation of the equivalence principle (EP) in Earth's field of

$$\eta(\text{Be,Al}) = \frac{\Delta\vec{a}_\perp \cdot \hat{n}}{g \sin\delta} = (-0.2 \pm 2.8) \times 10^{-12} ,$$
$$\eta(\text{Be,Cu}) = \frac{\Delta\vec{a}_\perp \cdot \hat{n}}{g \sin\delta} = (-1.9 \pm 2.5) \times 10^{-12} . \quad (49)$$

Here we used $g = 981\,\text{cm/s}^2$ and $\delta = 1.67 \times 10^{-3}$ is the angle between local vertical and a line pointing to the center of Earth. The errors in our Be-Al and Be-Cu values are predominantly independent. We can combine these two results to conclude that any violation of the EP for Be and a composite body consisting of equal masses of Al and Cu is

$$\eta(\text{Be,Al/Cu}) = (-1.1 \pm 1.9) \times 10^{-12} . \quad (50)$$

1. Strong and electromagnetic energy

Here we adopt a classical (i.e., pre-QCD) point of view and consider the nucleons as elementary objects, so that the strong and electromagnetic (EM) energies are dominated by those involved in the internucleon forces. The fractional contributions of strong binding energy to the inertial masses of our Cu and Be test bodies are $f_S^{\rm Cu} = -9.158 \times 10^{-3}$ and $f_S^{\rm Be} = -6.685 \times 10^{-3}$, respectively. So the result in Eq. (49) implies

$$\eta_S = \eta(\text{Be,Cu})/(f_S^{\rm Be} - f_S^{\rm Cu}) = (-7.7 \pm 10.1) \times 10^{-10} . \quad (51)$$

The fractional contributions of EM energy to the inertial masses of our Cu and Be test bodies are $f_{\rm EM}^{\rm Cu} = +4.95 \times 10^{-4}$ and $f_{\rm EM}^{\rm Be} = +2.48 \times 10^{-3}$, respectively. So the result in Eq. (49) implies

$$\eta_{\rm EM} = \eta(\text{Be,Cu})/(f_{\rm EM}^{\rm Be} - f_{\rm EM}^{\rm Cu}) = (+9.6 \pm 12.6) \times 10^{-10} . \quad (52)$$

2. Weak-interaction energy

Haugan and Will [32] and Lobov [33] have calculated the weak-interaction component of the nuclear energy, based on the standard electroweak model. These two works considered only the N-N interactions and did not include the weak component of the masses of the nucleons themselves which we suspect will also make a significant contribution. We use the recent calculation of Lobov as it employs more realistic values of the nuclear and electroweak parameters. Lobov found that the fractional weak-interaction contribution to the inertial mass of a nucleus with mass A was

$$f_W = 10^{-8} \frac{NZ}{A^2} \left(1 + 0.125 \frac{N-1}{Z} + 0.16 \frac{Z-1}{N}\right) , \quad (53)$$

where N and Z are the neutron and proton numbers. Using this expression we found that the weak interaction alters the inertial masses of our Be and Cu bodies by 3.015 parts in 10^9 and 3.161 parts in 10^9, respectively. The results in Eq. (49) therefore verify that the weak interaction obeys the EP to about 3.5 parts in 100. We note that had we used the earlier weak energy calculation of Ref. [32] our limit would have been improved by a factor of 4.

3. Gravitational binding energy

The gravitational binding energy of laboratory objects is much too small to permit laboratory tests of the EP for gravitational binding energy. Nordtvedt [34] pointed out that it can be tested using the Earth-Moon system. Gravitational binding energy reduces Earth's mass by about 5 parts in 10^{10} but has a much smaller effect, about 2 parts in 10^{11}, on the Moon's mass, so that an anomaly in the gravitational properties of gravitational binding energy would produce a difference in the accelerations of Earth and the Moon toward the Sun that could be detected by lunar laser ranging.

Nordtvedt [7] also pointed out that the lunar ranging test is, by itself, ambiguous; Earth and the Moon differ in their composition as well as in their masses, so that the Earth-Moon acceleration difference tests two things at once. These two tests can be separated by studying the differential accelerations toward the Sun of laboratory-sized "scale models" of Earth and the Moon, which would have negligible gravitational binding energy but the same composition-dependent accelerations as the real Earth and Moon.

We approximated this test as follows. The compositions of Earth and the Moon differ primarily because Earth has a Fe/Ni core and a Si/Al crust, while the Moon consists mainly of Si/Al material. Our Si/Al test bodies approximated the material of Earth's crust and the

Moon, while our Cu test bodies simulated the Fe/Ni core (it was obviously not practical to use Fe or Ni). Therefore any composition-dependent differential acceleration of Earth and the Moon toward the Sun is constrained by the results in Eq. (34) to be

$$\frac{\Delta a_{\rm comp}}{a_{\rm Sun}} \approx \frac{-\Delta a^{\odot}({\rm Si/Al\text{-}Cu})}{a_{\rm Sun}} \frac{M_{\rm core}}{M_{\rm Earth}}$$

$$= (-1.6 \pm 2.2) \times 10^{-12} , \qquad (54)$$

where $\Delta a_{\rm comp}$ is the differential Earth-Moon acceleration arising from a composition-dependent interaction, $a_{\rm Sun} = 0.593$ cm/s^2 is Earth's acceleration toward the Sun, and $M_{\rm core}$ and $M_{\rm Earth}$ denote the masses of Earth's core and the entire Earth, respectively. We assume that $M_{\rm core}/M_{\rm Earth} = 0.32$ [35]. Lunar laser ranging [8] has established that

$$\frac{\Delta a_{\rm comp} + \Delta a_g}{a_{\rm Sun}} = (+2.7 \pm 6.2) \times 10^{-13} , \qquad (55)$$

where Δa_g is the differential acceleration ascribed to gravitational binding energy differences. Combining our results with the lunar ranging data, we conclude that $\Delta a_g/a_{\rm Sun} = (+1.9 \pm 2.3) \times 10^{-12}$ which tests the EP for gravitational binding energy at the level of

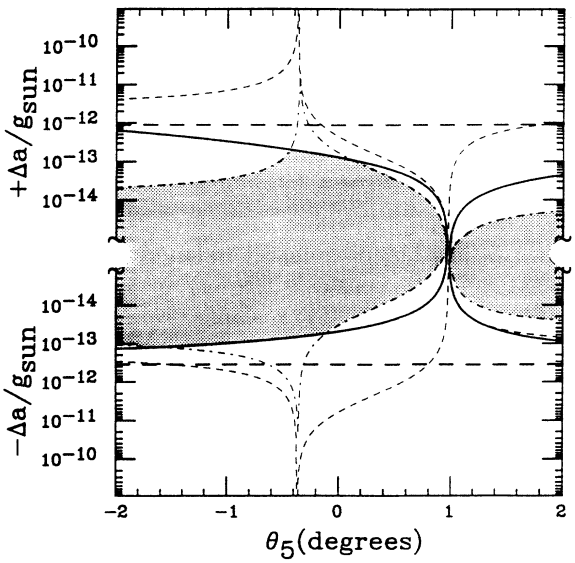

FIG. 19. 1σ limits on differential Earth-Moon acceleration toward the Sun. Lunar laser-ranging limits [8] on $(\Delta a_{\rm comp} + \Delta a_g)/a_{\rm Sun}$ are shown as heavy dashed lines. The curved lines are upper bounds on $\Delta a_{\rm comp}$ from a vector interaction as a function of θ_5, the parameter specifying the vector "charge." The heavy solid curves show the constraint obtained from our Be-Cu, Be-Al, and Si/Al-Cu data; the light dashed and dash-dotted curves show constraints inferred from the data of Refs. [1] and [2], respectively. (The data of Ref. [2] require $-1.1 \times 10^{-13} < \Delta a_{\rm comp}/a_{\rm Sun} < +2.1 \times 10^{-13}$ for θ_5 values lying outside the range of this plot.) For an *arbitrary* vector interaction, our work plus that of Ref. [2] imply $\Delta a_{\rm comp}/a_{\rm Sun} = (+0.4 \pm 1.7) \times 10^{-13}$. This constraint is sufficiently tight that the uncertainty in $\Delta a_g/a_{\rm Sun}$ is dominated by the lunar laser-ranging result.

$$\eta_G = \frac{1}{f_G^e - f_G^m} \frac{\Delta a_g}{a_{\rm Sun}} = (-4.0 \pm 4.8) \times 10^{-3} , \qquad (56)$$

where $f_G^e = -5.0 \times 10^{-10}$ and $f_G^m = -2 \times 10^{-11}$ are the fractions of Earth's and the Moon's masses that reside in gravitational binding energy.

We obtain a tighter constraint if composition-dependent forces are restricted to vector interactions (see Sec. V A above). Then, following the reasoning outlined in Ref. [11], our Be-Al, Be-Cu, and Si/Al-Cu results given in Eqs. (49) and (34), together with the classical results of Refs. [1,2], restrict the parameter $\alpha_5(\theta_5)$ defined in Eq. (3) and require any composition-dependent Earth-Moon acceleration difference (see Fig. 19) to lie within the 1σ limits $\Delta a_{\rm comp}/a_{\rm Sun} = (+0.4 \pm 1.7) \times 10^{-13}$; when our constraint is combined with the result in Eq. (55), we find $\Delta a_g/a_{\rm Sun} = (+2.4 \pm 6.4) \times 10^{-13}$ which corresponds to an EP test for gravitational binding energy at the level of

$$\eta_G = (-0.5 \pm 1.3) \times 10^{-3} . \qquad (57)$$

C. Anomalously large neutrino scattering cross sections?

Weber [9] claims to have detected the *pp* neutrinos from the Sun using a torsion balance that compared the accelerations of single-crystal sapphire and amorphous Pb test bodies toward the Sun. He argued that the solar neutrinos transferred detectable momentum to his sapphire test bodies because the neutrinos scattered coherently from the entire crystal giving a cross section that was $\sim 10^{23}$ times larger than the standard expectation. His theoretical arguments [36] that neutrinos with wavelengths much larger than the crystal lattice spacing scatter with cross sections proportional to the square of the total number of scatterers have been refuted elsewhere (see, for example, Refs. [10,37]). Here we address Weber's claim that he has verified his theory *experimentally* by using neutrinos from the Sun. Even though our test bodies were far from optimized for testing Weber's result (compared to the bodies used by Weber, the square of the number of scatterers was smaller by a factor of 17 and the Debye temperature was lower by a factor 1.6), we had sufficient sensitivity to make a decisive test of Weber's claim that solar neutrinos apply an appreciable force to single-crystal test bodies.

Our Si/Al test bodies contained 6.3 g dislocation-free, zone-refined, single crystals of Si prepared according to current practice for assuring long-range lattice coherence [38]. Although Si has a lower Debye temperature than sapphire (640 K vs ≈1000 K) our Si crystals are expected to be more nearly dynamically perfect; even the best available sapphire material does not maintain lattice coherence over distances of 1 cm [38]. Thus our Si/Al-Cu experiment formed a test that was conceptually equivalent to Weber's measurement. If Weber's result and proposed mechanism were correct, we should have, using Eq. (8) of Ref. [9], observed a force on our Si crystal, $F_{\rm Weber} = 2.7 \times 10^{-8}$ dyn, that pointed away from the

Sun. The corresponding solar signal would be equivalent to $\Delta a^{\odot}(\mathrm{Si/Al\text{-}Cu}) = -3.0\times10^{-9}$ cm/s^2. Instead we saw a signal [see Eq. (34)] of less than -5.0×10^{-12} cm/s^2 (2σ limit on Si being repelled by the Sun). So we establish a 2σ upper limit on the force exerted by solar neutrinos, F_{expt}, that is smaller than that predicted by Weber by a factor

$$\frac{F_{\mathrm{expt}}}{F_{\mathrm{Weber}}} \leq \frac{1}{530} . \tag{58}$$

Our test of Weber's ideas has somewhat better sensitivity than recent work by Franson and Jacobs [39], and is complimentary because we used a different crystalline material (Si instead of sapphire). We conclude that Weber's claim of enhanced scattering of solar neutrinos has been ruled out by direct *experimental* tests.

VI. FUTURE PROSPECTS

The history of some modern tests of the equivalence principle is shown in Fig. 20; a comprehensive review of searches for composition-dependent forces up through 1990 may be found in Ref. [31]. With the publication of these results we have reached the practical sensitivity limit of our present apparatus. We are now designing a new rotating balance that should give substantially improved statistical and systematic errors.

In addition we have developed a stationary balance surrounded by a rotating 3-ton uranium source. This instrument allows us to probe Yukawa interactions with ranges down to 1 cm and gives sensitivity to interaction "charges" for which Earth (having essentially equal numbers of neutrons and protons) is neutral. Results from this experiment will be reported in a separate publication.

There remains a large, essentially unexplored, region corresponding to interactions with ranges less than 1 mm. In this regime the usual techniques of experimental gravity are not applicable and new ideas will probably be required before substantial progress can occur. The new techniques of laser-cooled atomic fountains [40] and trampolines [41], microfabrication [42], and atomic force microscopy [43] may provide access to this short-range regime.

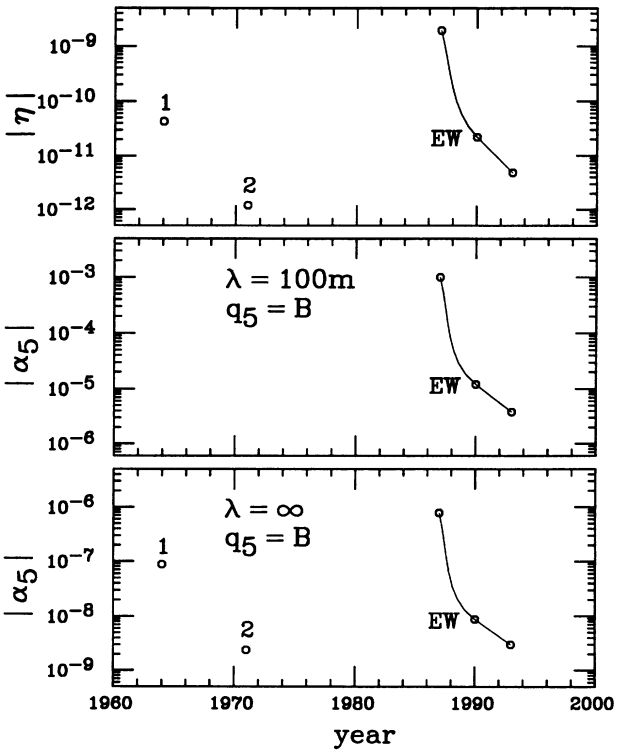

FIG. 20. Recent progress in equivalence principle tests. Top: 2σ upper limits on $|\eta|$ versus the year of publication. Center: corresponding 2σ upper limits on $|\alpha_5|$ for an infinite-ranged vector interaction coupled to baryon number. Bottom: 2σ upper limits on $|\alpha_5|$ for a $\lambda = 100$ m vector interaction coupled to baryon number. The points labeled EW show results of our group. Other results are labeled by the reference number.

ACKNOWLEDGMENTS

Phil Williams designed and built the very successful turntable-rate controller. The elegant gravitational and Yukawa multipole moment program MULTI, which was invaluable in designing pendulums and gradient compensators, was written by Tim Bast. We relied heavily on the skills of the instrument makers in the Physics Department and Nuclear Physics Laboratory Machine Shops. Geoff Greene and Richard Deslattes kindly supplied us with the dynamically perfect single-crystal silicon used in our Si/Al test bodies. We thank Christopher Stubbs for suggesting that we look for a galactic signal in our data. Finally, we are most grateful to the National Science Foundation for primary financial support via Grant No. PHY9104541 and to the Department of Energy for for supporting the Nuclear Physics Laboratory where this work was conducted.

[1] P.G. Roll, R. Krotkov, and R.H. Dicke, Ann. Phys. (N.Y.) **26**, 442 (1964).

[2] V.B. Braginsky and V.I. Panov, Zh. Eksp. Teor. Fiz. **61**, 873 (1971) [Sov. Phys. JETP **34**, 463 (1972)].

[3] Torsion balances are sensitive only to *horizontal* accelerations. At a latitude of 45°, the gravitational acceleration toward the Sun is 2.82 times smaller than the horizontal component of the acceleration due to Earth's gravity.

[4] T. Damour and A.M. Polyakov, Nucl. Phys. B (to be published).

[5] C.W. Stubbs, Phys. Rev. Lett. **70**, 119 (1993).

[6] G. Smith, E.G. Adelberger, B.R. Heckel, and Y. Su,

Phys. Rev. Lett. **70**, 123 (1993).
[7] K. Nordtvedt, Phys. Rev. D **37**, 1070 (1988).
[8] J.O. Dickey *et al.*, Science (to be published).
[9] J. Weber, Phys. Rev. D **38**, 32 (1988).
[10] L. Stodolsky, in *Proceedings of TPAUP '89 Workshop*, edited by A. Bottino and P. Monacelli (Editions Frontieres, Gif-sur-Yvette, France, 1989), p. 297.
[11] E.G. Adelberger *et al.*, Phys. Rev. D **42**, 3267 (1990).
[12] A.R. Edmonds, *Angular Momentum in Quantum Mechanics* (Princeton University Press, Princeton, 1960).
[13] A ball bearing imperfection can produce effects at half the rotation frequency. We found no evidence for such $\omega_c/2$ modulations.
[14] Y. Su, Ph.D. thesis, University of Washington, 1992.
[15] T.M. Niebauer, M.P. McHugh, and J.R. Faller, Phys. Rev. Lett. **59**, 609 (1987).
[16] K. Kuroda and N. Mio, Phys. Rev. Lett. **62**, 1941 (1989).
[17] P.G. Nelson, D.M. Graham, and R.D. Newman, Phys. Rev. D **42**, 963 (1990).
[18] J.K. Hoskins, R.D. Newman, R. Spero, and J. Schultz, Phys. Rev. D **32**, 3084 (1985).
[19] C. Talmadge, J.-P. Berthias, R.W. Hellings, and E.M. Standish, Phys. Rev. Lett. **61**, 1159 (1988).
[20] T. Damour, in *Perspectives in Neutrinos, Atomic Physics and Gravitation*, edited by J. Tran Than Van, T. Damour, E. Hinds, and J. Wilkerson (Editions Frontieres, Gif-sur-Yvette, France, 1993), p. 465.
[21] See *Dark Matter in the Universe*, Proceedings of the Jerusalem Winter School for Theoretical Physics, Jerusalem, Israel, 1987, edited by J. Bahcall, T. Piran, and S. Weinberg (World Scientific, Singapore, 1987), Vol. 4.
[22] J. Binney and S. Tremaine, *Galactic Dynamics* (Princeton University Press, Princeton, 1987).
[23] C. Alcock *et al.*, Nature (London) **365**, 621 (1993).
[24] E. Aubourg *et al.*, Nature (London) **365**, 623 (1993).
[25] J. Primack, D. Seckel, and B. Sadoulet, Annu. Rev. Nucl. Part. Sci. **38**, 751 (1988).
[26] J.A. Frieman and B.-A. Gradwohl, Phys. Rev. Lett. **67**, 2696 (1991).
[27] K.L. Nordtvedt (private communication).
[28] P. Lubin *et al.*, Astrophys. J. Lett. **298**, L1 (1985).
[29] G.F. Smoot *et al.*, Astrophys. J. Lett. **396**, L1 (1992).
[30] J.P. Huchra, Science **256**, 321 (1992).
[31] E.G. Adelberger, B.R. Heckel, C.W. Stubbs, and W.J. Rogers, Annu. Rev. Nucl. Part. Sci. **41**, 269 (1991).
[32] M.P. Haugan and C.M. Will, Phys. Rev. Lett. **37**, 1 (1976).
[33] G.A. Lobov, Yad. Fiz. **52**, 1451 (1990) [Sov. J. Nucl. Phys. **52**, 918 (1990)].
[34] K. Nordtvedt, Phys. Rev. **170**, 1186 (1968).
[35] J.W. Morgan and E. Anders, Proc. Natl. Acad. Sci. (USA) **77**, 6973 (1980).
[36] J. Weber, Phys. Rev. C **31**, 1468 (1985).
[37] G.F. Bertsch and S.M. Austin, Phys. Rev. C **34**, 361 (1986).
[38] R. Deslattes (private communication).
[39] J.D. Franson and B.C. Jacobs, Phys. Rev. A **46**, 2235 (1992).
[40] M. Kasevitch *et al.*, Phys. Rev. Lett. **66**, 2297 (1991).
[41] C.G. Aminoff *et al.*, Phys. Rev. Lett. **71**, 3083 (1993).
[42] R.N. Kleiman *et al.*, Rev. Sci. Instrum. **56**, 2088 (1985).
[43] G. Binnig, Ultramicroscopy **42-44**, 7 (1992).

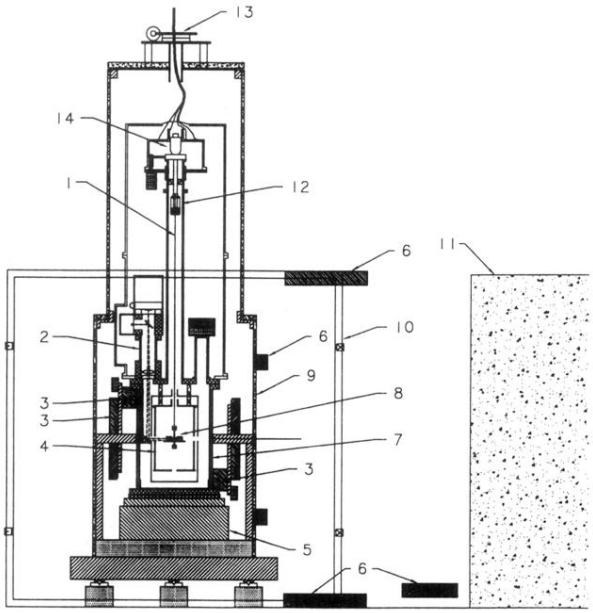

FIG. 1. Cross section of Eöt-Wash apparatus. 1, torsion fiber; 2, autocollimator; 3, rotateable gravity-gradient compensators; 4, magnetic shields; 5, turntable; 6, stationary gravity-gradient compensators; 7, vacuum vessel; 8, pendulum; 9, outer heat shield; 10, Helmholtz coils; 11, concrete block; 12, damper; 13, corotating cable clamp; 14, upper fiber attachment mechanism. The concrete block abuts the hillside wall of the laboratory and is 1.23 m high.

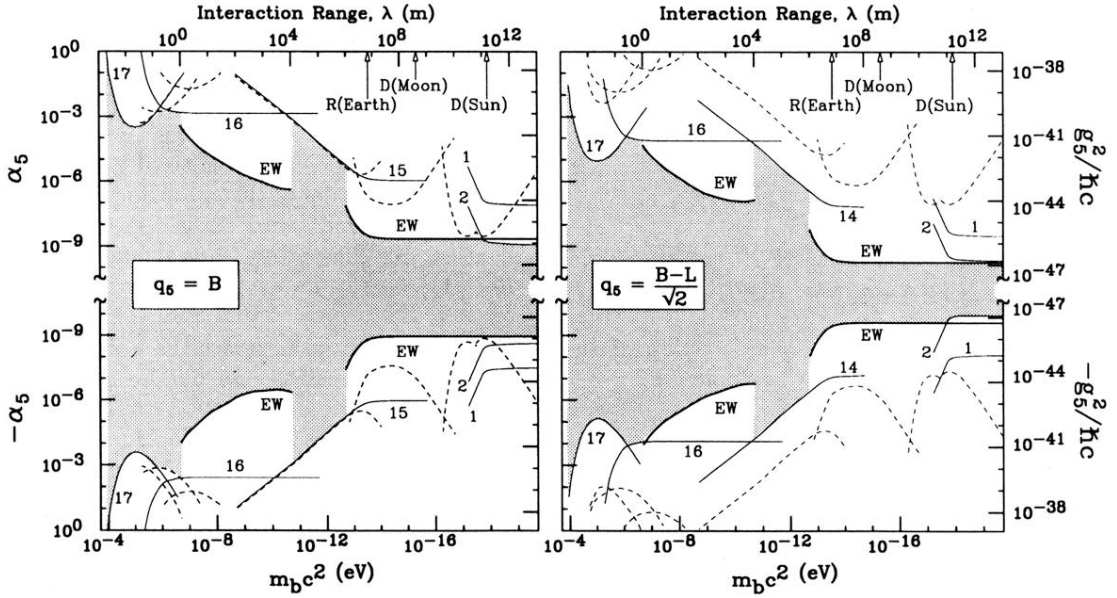

FIG. 16. 2σ upper limits on the coupling strength of a new Yukawa interaction as a function of the interaction range λ. Results are shown for possible charges of $q_5 = B$ and $q_5 = (B - L)/\sqrt{2}$. Heavy solid curves labeled EW are from this work. Light solid curves labeled by reference numbers are from other composition dependence and $1/r^2$ tests. Dashed curves are from tests of the $1/r^2$ law summarized in Ref. [19]. The experimentally allowed region is shaded in this and subsequent figures.

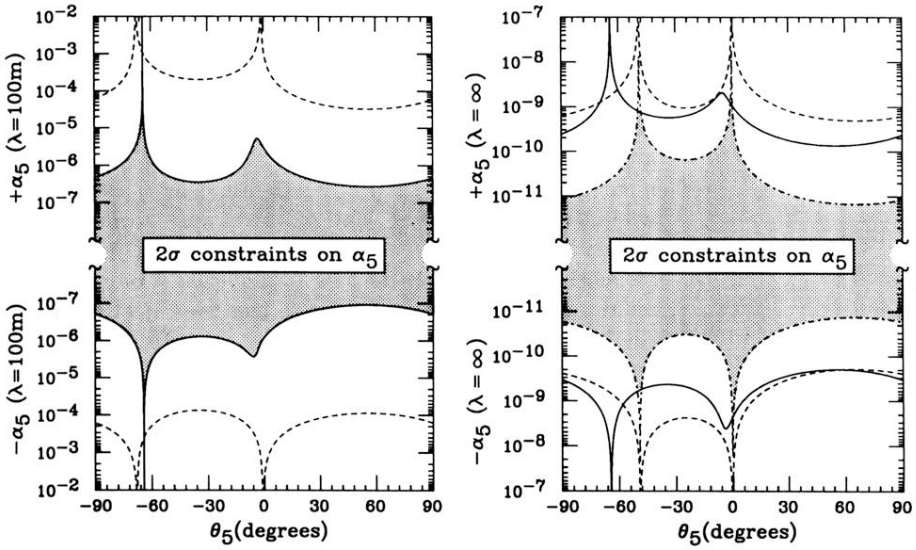

FIG. 17. 2σ upper limits on the coupling strength of a new Yukawa interaction as a function of θ_5 (a parameter that determines the vector charge of stable matter). Results are shown for two values of the range $\lambda = 100$ m and $\lambda = \infty$. The solid lines are from this work. The dashed lines in $\lambda = 100$ m plot show limits from the Pb-source experiment of Ref. [17]. The dashed and dash-dotted lines in the $\lambda = \infty$ plot are the results of the Princeton [1] and Moscow [2] experiments, respectively.

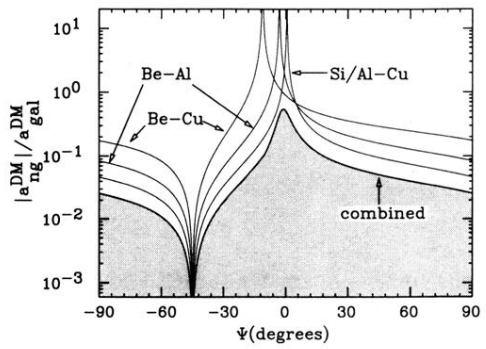

FIG. 18. 1σ constraints on the nongravitational acceleration of neutral hydrogen due to a hypothetical long-range scalar interaction with dark matter. These results are based on our data with Be, Al, Cu, and Si/Al test bodies and assume that R has the form given in Eq. (45). The vertical axis shows the ratio of the anomalous acceleration $|a_{\mathbf{ng}}^{\mathbf{DM}}|$ to the total $a_{\mathbf{gal}}^{\mathbf{DM}}$. The variable on the horizontal axis specifies the scalar charge of ordinary matter.

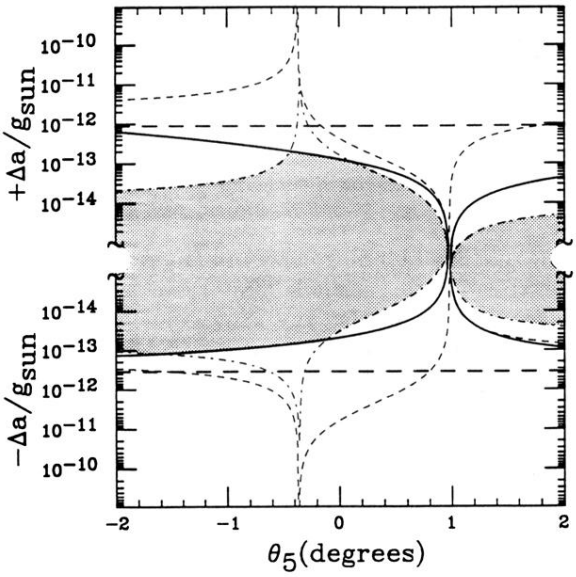

FIG. 19. 1σ limits on differential Earth-Moon acceleration toward the Sun. Lunar laser-ranging limits [8] on $(\Delta a_{\rm comp} + \Delta a_g)/a_{\rm Sun}$ are shown as heavy dashed lines. The curved lines are upper bounds on $\Delta a_{\rm comp}$ from a vector interaction as a function of θ_5, the parameter specifying the vector "charge." The heavy solid curves show the constraint obtained from our Be-Cu, Be-Al, and Si/Al-Cu data; the light dashed and dash-dotted curves show constraints inferred from the data of Refs. [1] and [2], respectively. (The data of Ref. [2] require $-1.1 \times 10^{-13} < \Delta a_{\rm comp}/a_{\rm Sun} < +2.1 \times 10^{-13}$ for θ_5 values lying outside the range of this plot.) For an *arbitrary* vector interaction, our work plus that of Ref. [2] imply $\Delta a_{\rm comp}/a_{\rm Sun} = (+0.4 \pm 1.7) \times 10^{-13}$. This constraint is sufficiently tight that the uncertainty in $\Delta a_g/a_{\rm Sun}$ is dominated by the lunar laser-ranging result.

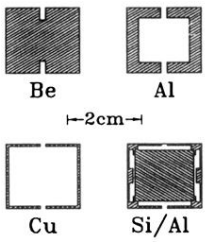

FIG. 3. Cross-sectional views of the test bodies. The symmetry axes of the cylindrical bodies lie vertically in the plane of the page.

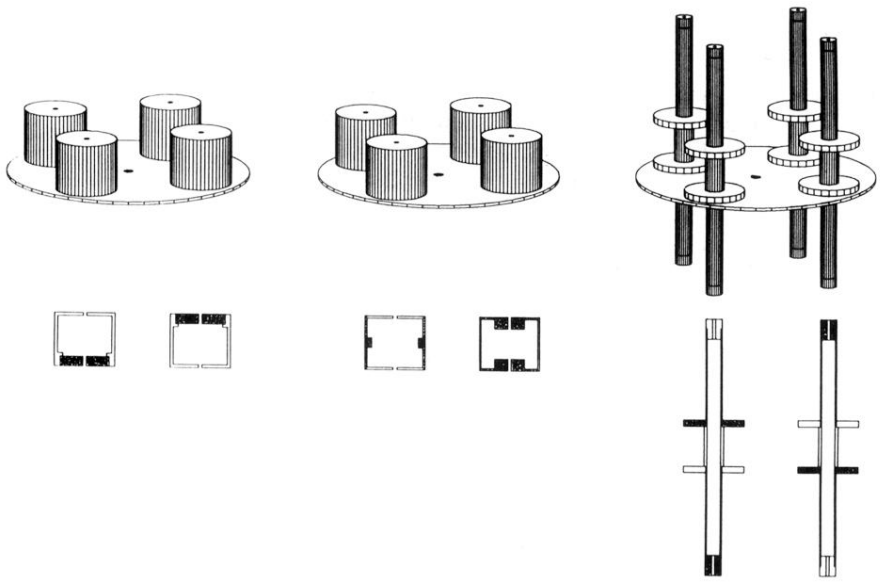

FIG. 6. Gravity gradiometers used in this work. Left: gradiometer with a large, calculable $\overline{q}_{21}$ moment that measures the laboratory Q_{21} gradient. Center: gradiometer with a large, calculable $\overline{q}_{31}$ moment that measures the laboratory Q_{31} gradient. Right: gradiometer with a large, calculable $\overline{q}_{41}$ moment that measures the laboratory Q_{41} gradient. The shaded areas in the cross-sectional views are Cu; the unshaded areas are Al.

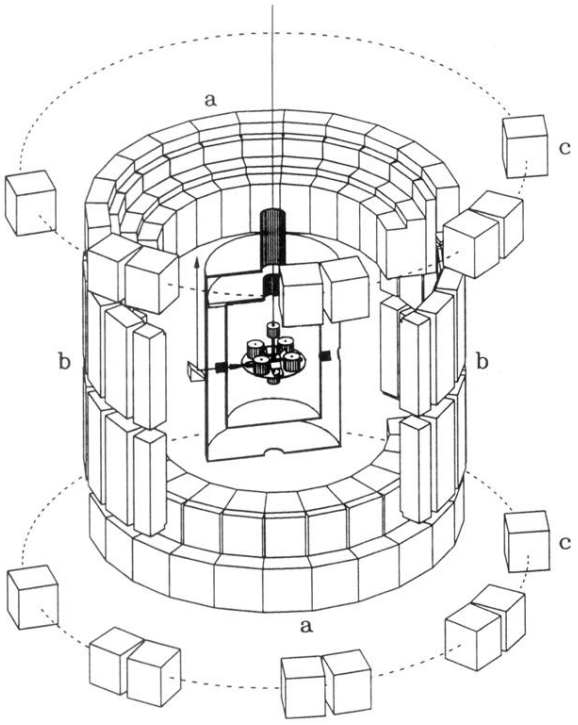

FIG. 8. Gravity-gradient compensators used to "flatten" the local gravitational field: *a*: Q_{21} compensator, *b*: Q_{22} compensator, *c*: Q_{31} compensator.